Climate Dynamics

Western North Pacific Modulation of ENSO through the Kuroshio Pathway

--Manuscript Draft--

Manuscript Number:	
Full Title:	Western North Pacific Modulation of ENSO through the Kuroshio Pathway
Article Type:	Original Article
Keywords:	ENSO, Victoria Mode, North Pacific Oscillation, Seasonal Footprinting Mechanism, Community Earth System Model
Corresponding Author:	Yu-heng Tseng, PH.D. NCAR Boulder, CO UNITED STATES
Corresponding Author Secondary Information:	
Corresponding Author's Institution:	NCAR
Corresponding Author's Secondary Institution:	
First Author:	Yu-heng Tseng, PH.D.
First Author Secondary Information:	
Order of Authors:	Yu-heng Tseng, PH.D.
	Chun Hoe Chow
	Ruiqiang Ding
	Jianping Li
Order of Authors Secondary Information:	
Abstract:	We investigate the origin of the extratropical forcing on El Niño-Southern Oscillation (ENSO) and explore the associated pathway in the western North Pacific using observations and the Community Earth System Model (CESM). The CESM successfully simulates the two dominant coupled modes of surface variability compared with the observation. The first mode of the combined empirical orthogonal function (CEOF) analysis represents the ENSO/Pacific Decadal Oscillation (PDO) variability, which expresses the zonal variability in the tropics and mid-latitudes. The second CEOF mode shows the North Pacific Oscillation (NPO)/Victoria Mode (VM) variability reflecting the footprint of the meridional variability through the tropical-extratropical teleconnection. Wavelet analysis for both the observation and CESM indicates that the first mode is dominated by interannual-scale variability, while the second mode is dominated by decadal-scale variability. These two leading modes can explain most of the North Pacific climate variability and are linked with each other. Using additional CESM model experiments, the impacts of ocean-atmosphere (O-A) variability in the Indo-Pacific Warm Pool (IPWP) are found to be critical in the tropical-extratropical teleconnection. The decadal-scale variability associated with the second CEOF mode is significantly reduced when the O-A variability of the IPWP is removed. Moreover, the O-A variability in the IPWP acts as a pivotal driver to modulate the NPO/VM patterns through the Kuroshio pathway and finally trigger some El Niño events. Further composite analysis shows that the O-A variability in the IPWP propagates into the Kuroshio-Oyashio Extension (KOE) region with the aid of intensive air-sea interaction along the Kuroshio. The SST variability in the KOE then further modulates the NPO through the heat flux exchange at a time scale of approximately 2 months, finally affecting El Niño through the Seasonal Footprint Mechanism (SFM). We confirm that this Kuroshio pathway, which modulates the NPO, and thus El Niño, is one effective dynamic process for the tropical-extratropical teleconnection within an integrated Pacific climate paradigm.
Suggested Reviewers:	L.H. LinHo Professor, National Taiwan University

	linho@as.ntu.edu.tw He is a well-known climate expert in the ENSO dynamics
	Fei-fei Jin U. Hawaii at Manoa jff@hawaii.edu He is a well-known climate expert in the ENSO dynamics
	Arthur J. Miller University of California, San Diego ajmiller@ucsd.edu He is a well-known oceanography/export in the PDO/ENSO and Pacific Climate Dynamics
	Shih Yu Wang Utah State University simon.wang@usu.edu He is an expert in ENSO prediction and atmospheric dynamics

Western North Pacific Modulation of ENSO through the Kuroshio Pathway

Yu-heng Tseng[1], Chun Hoe Chow[2], Ruiqiang Ding[3] and Jianping Li[3]

[1]*Climate and Global Dynamics Division, NCAR, Boulder, Colorado, USA*

[2]*Research Center for Environmental Changes, Academia Sinica, Taiwan*

[3]*State Key Laboratory of Numerical Modeling for Atmospheric Sciences and Geophysical Fluid Dynamics (LASG), Institute of Atmospheric Physics, Chinese Academy of Sciences, Beijing, China*

(Submitted to ***Climate Dynamics*** 5 May 2014)

Corresponding author: Dr. Yu-heng Tseng, Climate and Global Dynamics Division, National Center for Atmospheric Research, 1850 Table Mesa Dr., Boulder, CO80305, USA. Email: ytseng@ucar.edu.

Abstract

We investigate the origin of the extratropical forcing on El Niño–Southern Oscillation (ENSO) and explore the associated pathway in the western North Pacific using observations and the Community Earth System Model (CESM). The CESM successfully simulates the two dominant coupled modes of surface variability compared with the observation. The first mode of the combined empirical orthogonal function (CEOF) analysis represents the ENSO/Pacific Decadal Oscillation (PDO) variability, which expresses the zonal variability in the tropics and mid-latitudes. The second CEOF mode shows the North Pacific Oscillation (NPO)/Victoria Mode (VM) variability reflecting the footprint of the meridional variability through the tropical–extratropical teleconnection. Wavelet analysis for both the observation and CESM indicates that the first mode is dominated by interannual-scale variability, while the second mode is dominated by decadal-scale variability. These two leading modes can explain most of the North Pacific climate variability and are linked with each other. Using additional CESM model experiments, the impacts of ocean–atmosphere (O–A) variability in the Indo-Pacific Warm Pool (IPWP) are found to be critical in the tropical–extratropical teleconnection. The decadal-scale variability associated with the second CEOF mode is significantly reduced when the O–A variability of the IPWP is removed. Moreover, the O–A variability in the IPWP acts as a pivotal driver to modulate the NPO/VM patterns through the Kuroshio pathway and finally trigger some El Niño events. Further composite analysis shows that the O–A variability in the IPWP propagates into the Kuroshio–Oyashio Extension (KOE) region with the aid of intensive air–sea interaction along the Kuroshio. The SST variability in the KOE then further modulates the NPO through the heat flux exchange at a time scale of approximately 2 months, finally affecting El Niño through the Seasonal Footprint Mechanism (SFM). We confirm that this Kuroshio pathway, which modulates the NPO, and thus

36 El Niño, is one effective dynamic process for the tropical–extratropical teleconnection within an
37 integrated Pacific climate paradigm.
38

1 Introduction

The ocean–atmosphere (O–A) coupled system and its variation in the Pacific show a large impact on global weather and climate. For example, El Niño–Southern Oscillation (ENSO) is a particular mode of Pacific climate variability with strong coupling between the atmosphere and ocean in the tropical Pacific. The onset and evolution of an ENSO warm event is strongly related to the atmospheric and oceanic variations in the tropical Pacific (e.g., Bjerknes 1969; Wyrtki 1975). Current understanding of ENSO evolution and its development has advanced in the last few decades through many different ENSO theories and classifications. In general, there are two groups of theoretical explanations. First, ENSO variation is a self-sustained, unstable and naturally oscillating mode of the O–A system (e.g., Battisti 1988; Suarez and Schopf 1988; Battisti and Hirst 1989; Jin 1997). Second, ENSO is a stable mode triggered by atmospheric random "noise" forcing (Wang and Picaut 2013). In either case, the positive O–A feedback of Bjerknes (1969) is the triggering mechanism to initiate the development of El Niño resulting from a rapid collapse of the easterly trade winds (i.e., westerly wind burst). This unstable interaction between the trade winds and SST is further enhanced through changes in the ocean thermocline depth. The accumulated warm water in the western Pacific surges eastward in the form of equatorial downwelling Kelvin waves to initiate an El Niño event that matures in the December. However, the trigger of the Bjerknes feedback is thus far not clear, and the spring barrier is still a major constraint for ENSO prediction.

Several previous studies have found that the teleconnection between the tropics and mid-latitudes may drive ENSO variations through the "Seasonal Footprinting Mechanism" (SFM) proposed by Vimont et al. (2003). The SFM asserts that the second leading pattern of winter atmospheric circulation, the North Pacific Oscillation (NPO), and its variability over the North

Pacific can significantly impact the spring sea surface temperature (SST) anomalies in the central North Pacific (e.g., Vimont et al. 2009; Alexander et al. 2010; Furtado et al. 2012) by modifying the wind-stress fields and changing the net surface heat flux over the North Pacific. This SST footprint can subsequently persist into summer to force the overlying atmosphere, resulting in zonal wind stress anomalies triggering an ENSO event in the following winter. The NPO is defined as the second leading mode of winter sea level pressure (SLP) anomalies over the North Pacific (Walker and Bliss 1932; Rogers 1981). Hereafter, seasons refer to those of the Northern Hemisphere.

The spring SST footprint is commonly called the "Meridional Mode" (MM), showing an opposite-signed meridional SST anomalies gradient located in the central-eastern North Pacific, with one sign of the anomaly maximizing in the subtropics (10°–30°N) and the other located at the equator (Chiang and Vimont 2004). These processes eventually impact the tropics and trigger the ENSO variability (Chang et al. 2007). The MM is closely linked to the "Victoria Mode" (VM) of SST anomalies, which focuses on the whole North Pacific (Ding et al. 2014a, manuscript submitted to *J. Geophys. Res.*). These VM/MM patterns reach a maximum in late winter and early spring, and then persist until summer in the subtropics, where they can subsequently force the overlying atmosphere, initiating the westerly wind burst of the Bjerknes feedback at the equator which triggers the development of El Niño in the following winter. Several studies have shown that these patterns are indeed forced by the NPO variation (e.g., Alexander et al. 2010; Deser et al. 2012; Furtado et al. 2012; Ding et al. 2014a). Hereafter, we denote the year in which the VM/MM peaks in spring as year 0 and the preceding and following years as year −1 and 1, respectively. Therefore, the VM/MM patterns intensify after December(−1), associated with the NPO peak during winter(0) or D(−1)JF(0), and ENSO matures in December(0), sometimes

85 extending to D(0)JF(1). In general, the SFM emphasizes the forcing of the NPO, while the
86 VM/MM emphasizes the O–A process and its associated sea surface patterns prior to the
87 development of El Niño.

88 Ding et al. (2014a) further suggest that the VM may act as an effective pathway for
89 NPO-like atmospheric variability to drive ENSO variability via the SFM. They also find that
90 there exists another similar but independent influence of extratropical atmospheric variability in
91 the South Pacific on the occurrence of canonical El Niño events (Ding et al. 2014b, manuscript
92 submitted to *Clim. Dyn.*). In this paper, we focus on the North Pacific and the possible pathway
93 related to the origin of the VM/MM mode. Figure 1 shows the correlation map of Niño4 index in
94 January(1) and Pacific SST anomalies at different lags (only correlation coefficients significant
95 at the $p < 0.05$ level are shown) from Extended Reconstructed SST version 3b (ERSST.v3b)
96 observations (1957–2010). Niño4 index is chosen here because it closely connects the VM/MM
97 mode and the tropical warming. Similar patterns and correlations can be found using Niño3 or
98 Niño3.4 indices. The pattern of evolution shows the VM/MM mode in different months before
99 the mature phase of ENSO. We find good correlation between the SST anomalies and Niño4
100 index in the western North Pacific (WNP) and eastern Indian Ocean more than 9 months earlier
101 (left panel). The correlation is higher than 0.6 (significant at the $p < 0.05$ level) at the 12-month
102 lead time in the WNP. This high correlation feature also extends northeastward into the Kuroshio
103 Extension (KE) region, where O–A interaction is very strong (Kwon et al. 2010). Similar
104 patterns can also be found in the Hadley Centre SST data set (HadSST) (not shown).

105 Besides the VM/MM and its footprint on sea surface height variability, the North Pacific
106 Gyre Oscillation (NPGO) (Di Lorenzo 2008), several other regional studies have also found that
107 SST anomalies in the marginal seas of the WNP are colder than normal monthly climatology in

El Niño developing years [year(0)]. Hong et al. (2001) found that summer(0) SST anomalies in the East (Japan) Sea tend to be colder than during year(−1) prior to the developing year [year(0)]. They also found that SST anomalies during El Niño developing years are opposite to those during La Niña developing years. Similar cold SST anomalies in spring(0) have recently been further identified based on three independent long-term observational stations off the east coast of South Korea (Jo et al. 2014). These signals can be used as a useful predictor for El Niño development and are consistent with the correlation map in Fig. 1.

In particular, Wang et al. (2012) identified an SST anomaly dipole in the WNP during winter(0) is related to the development of El Niño in the following winter [winter(1)] and used it to enhance the ENSO forecast. They also observed a strong correlation between the SST anomalies dipole and the following ENSO in the marginal seas of the WNP (similar to Fig. 1). They thought that the spatial pattern in the WNP shares similar characteristics with the MM (Chiang and Vimont 2004; Chang et al. 2007; Zhang et al. 2009), except that the meridional SST anomalies gradient and low-level zonal wind anomalies occur in the western tropical Pacific. Indeed, the high correlation band shown in Wang et al. (2012) and Fig. 1 is a part of the VM, and the MM is also a part of the VM, in the central-eastern Pacific. These studies strongly support the notion that large-scale SST anomalies over the (subtropical/extratropical) North Pacific, associated with the winter NPO, are significantly related to El Niño 12–15 months later. However, it remains unclear as to how these regional WNP findings are linked to the basin-scale VM/MM and how these patterns are related to the NPO.

Looking further afield, many studies have suggested that the state of the Indian Ocean Dipole (IOD) can affect the onset and developing phases of El Niño in the Pacific (e.g., Annamalai et al. 2005; Izumo et al. 2010; Luo et al. 2008; Izumo et al. 2014), also consistent

131 with the correlation map in Fig. 1. Izumo et al. (2010) proposed that the IOD modulates the
132 strength of the Walker circulation in year(−1), which induces the westerly wind burst in the
133 tropical Pacific and then results in the subsequent El Niño event. In autumn(−1), the negative
134 IOD phase (warmer than the normal SST and higher precipitation in the eastern Indian Ocean)
135 enhances the Walker circulation of the Indo-Pacific Warm Pool (IPWP) region (easterly
136 anomalies over the Pacific and westerly anomalies over the Indian Ocean). In the western Pacific,
137 the easterly anomalies can force a downwelling Rossby wave and an upwelling Kelvin wave.
138 These waves increase the thermocline slope and induce a build-up of warm water in the western
139 Pacific, inducing a sudden collapse of anomalous zonal winds over the Pacific. They also found
140 that the linkage with IOD can help with ENSO predictability beyond the spring barrier and is
141 consistent with a positive warm water volume (WWV) anomaly preceding El Niño, as described
142 in Meinen and McPhaden (2000). However, is the IOD the major contributor to the onset of
143 ENSO? Is there any other local impact that can modulate the Hadley circulation in addition to the
144 enhanced Walker circulation?

145 In this paper, we seek to isolate the dominant source of extratropical forcing on ENSO and
146 explore its associated Kuroshio pathway. The significant impact of NPO on ENSO, or El Niño
147 Modoki (EM) specifically, has been extensively discussed recently based on the SFM, MM or
148 VM. However, what is the driving mechanism modulating the NPO? Anderson (2004, 2007)
149 found that the thermocline temperature anomalies in the western equatorial Pacific during
150 summer/autumn(−1), followed by the associated change of SLP over the subtropical central
151 North Pacific during winter(0), can affect the development of ENSO events in winter(1). When
152 the western equatorial heat content and the following SLP anomalies have the same sign, the
153 correlation disappears. Although Anderson found an interesting and promising relationship

between the western equatorial Pacific and subsequent ENSO events, no details with respect to the driving mechanisms or dynamics were described. Furtado et al. (2012) further found that a low-frequency modulation of the NPO comes from the low-frequency component of the EM phenomenon. However, they too provided no detail regarding the forcing mechanism of EM on the NPO and its direct linkage. Here, we clarify the pattern and variation of the tropical–extratropical teleconnection and its pathway using observational evidence and Community Earth System Model (CESM) sensitivity studies.

Section 2 introduces the CESM model experiments, the observational data, and the statistical methods. Section 3 describes and compares the dominant surface pattern and variability in the North Pacific. Section 4 details the origin of the ENSO precursor pathway resulting from the basin-scale tropical–extratropical teleconnection. Section 5 discusses the role of the Kuroshio pathway and how this framework explains the ENSO precursor signals in the literature. Finally, conclusions and suggestions in terms of future directions for further work are provided in section 6.

2 Numerical model experiments and observations

2.1 Community Earth System Model

Coupled model experiments are used to examine the influence of O–A interaction in the IPWP on the North Pacific variability. The CESM version 1 is used in this study (Gent et al. 2011). The default atmospheric model is based on the nominal 1° horizontal resolution (1.25°×0.9°), 26 vertical level, finite volume dynamic core of the Community Atmospheric Model 4 (CAM4), described in Neale et al. (2013). The land model is the Community Land Model version 4 (CLM4) and shares the same horizontal grid as CAM4 (Oleson et al. 2010;

Lawrence et al. 2011). The ocean component of CESM is the Parallel Ocean Program version 2 (POP2), which is a hydrostatic, free-surface, primitive-equation model formulated on a curvilinear orthogonal grid (Danabasoglu et al. 2012). The nominal 1° horizontal resolution version of the ocean component is used with 60 vertical levels. The latest version includes several new parameterizations [see Danabasoglu et al. (2012) for further details]. The sea-ice model is the updated Los Alamos Sea Ice Model version 4 (CICE4) and shares the same horizontal grid as POP2 (Hunke and Lipscomb 2008). It is a dynamic–thermodynamic model that includes a subgrid-scale ice thickness distribution. The most recent improvements include a Delta-Eddington multiple scattering radiative transfer model to simulate the interactions between solar radiation and snow, sea ice, and melt ponds, and a parameterization for melt ponds that relates the pond volume to the surface melt water flux (Holland et al. 2012).

2.2 Ocean–atmosphere variability forcing experiment of the Indo-Pacific Warm Pool

The IPWP has the warmest ocean water in the world (Wang and Mehta 2008). It is characterized by persistently warm SST higher than 28°C, a threshold for atmospheric deep convection (Fu et al. 1994). The O–A interaction is intensive in this region and the warm water is mainly formed by the ocean dynamics with the aid of atmospheric processes (Ramanathan and Collins 1991; Waliser and Graham 1993; Clement et al. 2005). According to the classic Clausius–Clapeyron relation (that is, surface saturation vapor pressure varies exponentially with SST), the strength of deep convection is very sensitive to changes in SST in the IPWP region. Even small variations in the SST can cause large changes in the atmospheric convection due to the warm ocean, which in turn can dramatically change atmospheric divergence locally, and further modify large-scale wave activity and atmospheric heating globally (Sardeshmukh and Hoskins 1988; Neale and Slingo 2003). For example, Wang and Xie (1998) demonstrated that

199 the mean state of warm SST in the IPWP favors O–A coupled unstable modes on the
200 intraseasonal time scale and thereby sustains the Madden–Julian Oscillation. Neal and Slingo
201 (2003) closely related the large convective activity over the Maritime Continent to the
202 large-scale variations in the climate system. These works point out that the IPWP is an important
203 source of energy for driving atmospheric circulation (Wang and Mehta 2008). Some previous
204 studies further indicate that the interannual variability of SST over the IPWP region may have a
205 positive feedback effect on the ENSO cycle (Solomon and Jin 2005; Chang et al. 2009). Mehta
206 and Fayos (2005) also illustrated that the decadal to multi-decadal IPWP variability can
207 modulate the interannual variability of ENSO. However, the detailed variation/pathway of the
208 IPWP impact on the ENSO evolution has not been well documented or understood.

209 Here, we demonstrate the O–A variability in the region of the IPWP is the dominant driver
210 for triggering some major El Niño events. Two sensitivity experiments are performed to remove
211 the local IPWP variability using the CESM, in addition to the "CESM control" simulation. In
212 order to explore the sensitivity of O–A variability in the IPWP, we design a "$Wind_{clim}$"
213 experiment which replaces the time-varying surface wind stress in the IPWP region by a constant
214 climatological wind field when forcing the ocean within the coupler. The IPWP is defined by the
215 rectangular box labeled in Fig. 2. This region is chosen based on the correlation map in Fig. 1
216 where the observed SST anomalies within this box leads the January(1) Niño4 index (similar for
217 other ENSO regions) by 9–15 months. The negative correlation has a value as high as 0.5–0.6,
218 implying the cold anomaly as observed previously. The other "SST_{clim}" experiment involves
219 replacing the time-varying SST by a constant climatological SST in the IPWP region when
220 forcing the atmosphere from the coupler. Note that this IPWP box is similar to the region where
221 deep convection commonly occurs in Izumo et al. (2010, 2014) prior to ENSO. However, Izumo

et al. (2010, 2014) did not explicitly connect the deep convection to the other off-equatorial precursor signals, such as the coldness in the WNP or the VM/MM mode. Here, we clarify that the O–A variability in the IPWP also initiates the modulation effect of the NPO on El Niño, in addition to the accompanying equatorial ENSO dynamics due to the change of Walker circulation. This tropical–extratropical pathway exists concurrently with the equatorial ENSO recharge–oscillator dynamics, but has a shorter time scale to initiate the NPO-modulated VM/MM mode.

Figure 2 shows the standard deviation of surface temperature (left panel) and surface wind stress (right panel) with masked lands for three numerical experiments. The surface temperature above the ocean in CAM4 is essentially close to the SST in POP2. Both climatological forcing fields used in the $\text{Wind}_{\text{clim}}$ and SST_{clim} experiments are obtained from the yearly averaged CESM control simulation so that the standard deviations of surface temperature and surface wind stress are nearly zero. We also do not see any boundary issue introduced by modifying the forcing field within the box. The global variations for both experiments are also similar to the control simulation (top). All simulations are branched from a preindustrial (AD1850) control experiment and integrated for 150 years to ensure the quasi-steady statistical results.

The two sensitivity experiments are designed so that they can still maintain the strength of mean Walker circulation and the modeled climatological Bjerknes feedback (Bjerknes 1969). This design makes sure the ENSO feature/behavior remains unaltered. In order to ensure there is no change in the Bjerknes feedback, which triggers the onset of ENSO regardless of ENSO type, we show a scatter diagram of averaged zonal wind speed in the observation (or wind stress in the CESM) vs. Niño4 SST anomalies (160°E–150°W) in Fig. 3. Both axes are normalized by their respective standard deviations. The surface wind changes can affect the thermocline structure

along the equator. On the other hand, the SST anomalies can also modify the wind convergences. This interactive coupling strength can be estimated by the slope of the linear fit for the scatter plot, Δ(zonal wind stress anomalies)/Δ(SST anomalies). There is no significant change in the O–A coupling strength among these CESM simulations (~15% weaker change only in the $Wind_{clim}$ simulation, and no change visually in the SST_{clim} simulation). This confirms the robustness of our model sensitivity setting that the surface zonal wind and the coupling strength of Bjerknes feedback in the tropical Pacific are not modified too greatly, which may potentially lead to different tropical ENSO intensities.

Figure 4 compares the averaged O–A coupling differences between the two experiments and the control simulation in the defined IPWP region. In the SST_{clim} experiment, where the forced SST input in the atmospheric model is replaced by the climatological SST, the only significant changes are the surface temperature (Fig. 4b) and sensible heat flux (Fig. 4d). The change in the latent heat flux (Fig. 4c) and surface wind (Fig. 4g) are small because the temperature here is uniformly warm in general and there is no strong temperature gradient that can drive significant boundary layer wind and atmospheric convergence (Lindzen and Nigam 1987). The feedback effect of the O–A interaction on the ocean is also weak (virtually no change in the ocean surface velocity). In the $Wind_{clim}$ experiment, the wind change affects the local surface ocean current and thus the SST. In general, this climatological wind forcing removes the large O–A variability and coupling driven by the variable wind and its associated wind stress. The surface latent heat (Fig. 4c) and sensible heat fluxes (Fig. 4d) also change accordingly, which causes large changes in precipitation and evaporation (Figs. 4e, f). In general, the SST_{clim} experiment is performed like a one-way forcing to the atmosphere, with no significant atmospheric feedback to the ocean. In the $Wind_{clim}$ experiment, the local air–sea interaction is limited and constrained. Removing the

surface wind variability reduces the O–A interaction, thus suppressing any potential teleconnection related to the heating source in this IPWP region.

2.3 Observational data

Two observational datasets for the period 1957–2010 are used here for comparison. The monthly SLP, surface wind components, surface latent heat flux, air temperature and wind vectors are from the National Centers for Environmental Prediction–National Center for Atmospheric Research (NCEP–NCAR) reanalysis project (Kalnay et al. 1996; Kistler et al. 2001) on a 2.5°×2.5° horizontal grid resolution and 17 vertical pressure levels ranging from 1000 to 10 hPa. The ERSST.v3b data are from the National Climatic Data Center on a 2°×2° horizontal grid (Smith et al. 2008). All relevant Niño indices are calculated from the ERSST.v3b data based on the standard definition. The representation of the NPO is defined according to Linkin and Nigam (2008).

2.4 Statistical methods

The combined empirical orthogonal function (CEOF) is used to clarify the covariance shared by different variables. Here, we use CEOF to analyze the covariability between the SLP and SST anomalies, which can better explain the O–A dynamical links in the Pacific. The anomalies in this study refer to the anomalies with respect to the monthly climatological mean. To emphasize the interannual and large-scale pattern variability, we apply the 9-month running mean to both the SLP and SST anomalies time series using the interpolated resolution. The resolution is 5° for the SLP anomalies and 4° for the SST anomalies in the observational data. In the model, the resolution is approximately 5° and 3°, respectively. Prior to the analysis of CEOF, the SST anomalies are normalized by the domain average standard deviation and the SLP anomalies are normalized along each latitude by the standard deviation at that latitude.

The possible influence of the heat source in the IPWP on the Pacific climate patterns may not be stationary and the time scales may vary. We therefore use wavelet analyses that require no assumption of stationarity to determine the dominant modes of variability in frequency and how those modes vary over time (Torrence and Compo 1998). We use the Morlet wavelet function. The 5% significance (or 95% confidence) level is determined based on a red-noise background. For comparison, the spectra shown in this study are normalized by the total data number divided by the data variance.

3. The dominant surface pattern and variability in the North Pacific

3.1 Spatial pattern

Figure 5 compares the two leading CEOF modes from the observation and model. The columns from left to right are the observation, CESM control, and the $Wind_{clim}$ and SST_{clim} experiments, respectively. The leading CEOF mode (CEOF1) of SLP anomalies in the Pacific is the Aleutian Low (AL), the semi-permanent low pressure winter center over the Aleutian Islands caused by planetary waves, in association with another strong pressure high near the IPWP region and another strong pressure low near the eastern equator. The spatial distributions are all similar between the observation and models, but the models can explain higher variances than the observation. The canonical ENSO/PDO pattern emerges in all CEOF1 of SST anomalies with warm anomalies in the cold tongue from the central-eastern tropical Pacific and cold anomalies in the western Pacific Ocean, which extend to the central Pacific in the mid-latitudes. In the mid-latitudes, the modeled strength is slightly weaker, although the associated SST anomalies variability pattern resembles the observed PDO pattern (Mantua et al. 1997; Zhang et al. 1997). In the tropics, the modeled positive ENSO anomalies seem to be stronger and extend more

zonally in the model results compared to the observation.

The second CEOF mode (CEOF2) of SLP anomalies in the North Pacific presents a typical meridional dipole structure of the NPO in the central-eastern Pacific, with positive anomalies in the north above 40°N (over the Aleutian Islands) and negative anomalies in the south between 0° and 40°N (over Hawaii). There is another weak pressure low in the subtropical WNP, which has drawn only minor attention previously (Anderson 2007). This NPO pattern is very similar to that reported earlier (Linkin and Nigam 2008; Furtado et al. 2012) and is a robust winter atmospheric feature. The models also show a similar NPO structure to the observation. In addition, the CEOF2 of the SST footprint resembles the VM/MM mode described above (Bond et al. 2003; Di Lorenzo et al. 2008; Ding et al. 2014a), with a region of negative SST anomalies extending from the WNP to the KE, encircled by warm SST anomalies around the North Pacific coast reaching the central tropical Pacific (Fig. 5, bottom). The modeled CEOF2 patterns are also similar to the observation, with a stronger footprint than the observation in the mid- to high latitudes.

Comparing the two CESM sensitivity experiments with the control simulation, the spatial patterns and their relevant variances do not change too much, as expected. These two experiments are designed by only removing the interannual variability of the IPWP air–sea interaction, to ensure the dominant patterns are not significantly altered. In the $Wind_{clim}$ experiment, we find a larger change in the patterns and strengths than in the SST_{clim} experiment. The variances of CEOF1 and CEOF2 in $Wind_{clim}$ drop from 38.0% to 34.5% and 12.0% to 9.6%, respectively. These variance and pattern changes are quite robust and consistent, even if we change the analysis period based on the results of the last 50 or 100 years. This implies a potentially larger suppression of the O–A interaction in the $Wind_{clim}$ simulation than in the SST_{clim} simulation, as described in section 2.2. These results also confirm that the underlying

dynamics in the sensitivity experiments used to generate the two leading modes remain active, but the relevant dynamics are slightly modified, which is further discussed below, in section 3.2.

3.2 Long-term variability associated with the spatial pattern

We find the pattern of CEOF1 SST shows a typical ENSO/PDO pattern, while the CEOF2 SST shows a typical VM/MM pattern, from the above section. Several studies have indicated these patterns are subject to the atmospheric forcing of the AL and NPO, respectively (e.g., Furtado et al. 2012; Ding et al. 2014a). Figure 6 shows the lag-correlation between the associated PC1/PC2 of the CEOF patterns and Niño3 index, as well as the EMI index, defined in Ashok et al. (2007). The positive (negative) *x*-axis means PC1/PC2 leads (lags) Niño3 or EMI index. In the observation, the temporal evolution of PC1 is highly correlated with Niño3 index (R=0.86; significant at the $p < 0.05$ level) and marginally correlated with EMI index (R=0.37; significant at the $p < 0.05$ level) at around the one-month lag time. All correlations discussed hereafter are significant at the $p < 0.05$ level unless otherwise stated. This indicates the spatial pattern of CEOF1 corresponds directly to the canonical ENSO variability. Note that the one month lead–lag may not be significant when the 9-month running mean is applied in the CEOF analysis. The temporal evolution of PC2 leads the time series of PC1 by 11 months (R=0.56), showing that the appearance of the second mode ahead of ENSO occurrence (Furtado et al. 2012) and the spatial pattern of CEOF2 can be seen as a precursor signal of ENSO. This relation also explains the lead–lag relation of PC2 and Niño3 at R=0.45 when the PC2 leads Niño3 by 9 months. In general, the PC1 and Niño3 index occur almost simultaneously. The correlation of PC1 with Niño3.4 is even higher at 0.90 (not shown). Our results confirm that ENSO/PDO is indeed a coupled tropical and extratropical variability while the typical Niño3.4 signal is a particular expression in the tropics (Zhang et al. 1997).

359 Of particular interest is the finding that PC2 leads EMI by 5 months at R=0.61 (shorter than
360 PC2 leading Niño3 by 9 months at R=0.45), which implies EM may be a direct footprint
361 resulting from the PC2 patterns, consistent with the previously discussed influence of the
362 NPO-forced VM/MM mode on EM (Ding et al. 2014a). The connection between the CEOF2
363 pattern and canonical ENSO (represented here by Niño3) may be the direct cause and effect
364 through CEOF1. The evolution can be seen in Fig. 1, where the CEOF1 SST pattern is similar to
365 Fig. 1f and the CEOF2 SST pattern is similar to Fig. 1c. Specifically, the warming in the central
366 Pacific (i.e., EM) may result from two different processes: one related closely to the surface O–A
367 interaction and the extratropical impact of the NPO; and the other related to the tropical
368 recharge–oscillator mechanism (Wang and Wang 2013; Chen et al. 2014, manuscript submitted
369 to *J. Clim.*). These two processes are not so easy to distinguish from the surface signatures in the
370 central tropical Pacific. Thus, the EMI index or the most recent EOF of SST-based index (e.g.,
371 Takahashi et al. 2011) may not be appropriate to separate the dynamical differences between
372 them. We will discuss this point further in a follow-up paper.
373 Figures 6b–d also show similar lag-correlations in the model experiments. The modeled
374 lag-correlations compare reasonably well with the observation. The high correlations of
375 approximately 0.95 between PC1 and Niño3 index show the ENSO variability can be well
376 represented by the basin-scale change of PC1 in the models (Deser et al. 2012). We need to be
377 mindful that the higher correlation between PC1 and EMI in all model simulations than that in
378 the observation may be misleading because this comes directly from the misrepresentation of the
379 westward elongation of canonical ENSO in the models (see modeled CEOF1 pattern in Fig. 5).
380 In addition, this causes the leading relationship of PC2 to EMI and Niño3 in the model to be less
381 clear due to the zonally elongated CEOF1 pattern. Thus, the leading relation of PC2 to Niño3 is

382 actually similar to the fact that PC2 leads PC1 (or ENSO) in the models.

383 Since the modeled tropical warming of ENSO is slightly shifted, we focus on the
384 relationship between the two dominant modes (PC1 vs. PC2). Reasonable relationships of the lag
385 time and correlation are still maintained in the CESM control (R=0.39 at 12 months lag) and the
386 two sensitivity experiments (R=0.46 at 14 months lag for $Wind_{clim}$ and R=0.42 at 9 months lag
387 for SST_{clim}). Some minor changes are as we expected. These results show that the sensitivity
388 experiments do not significantly alter the characteristics of the modeled patterns and the
389 associated relations. However, the O–A interaction in the IPWP indeed modifies the strength and
390 variability of the North Pacific coupling. The modeled ENSO precursors associated with PC2 is
391 a robust feature in the CESM with a shorter response time than the observation (Deser et al.
392 2012). Our results also confirm the SFM can be well represented in all CESM simulations. When
393 the anomalous low pressure is strengthened around the southern lobe of the NPO, the anomalous
394 westerly winds over the central and eastern subtropical Pacific reduce the wind speed and
395 upward latent heat flux, thereby warming the underlying ocean through December(−1) to
396 spring(0). The positive SST anomalies that extend into the tropical Pacific are then enhanced in
397 summer(0) and subsequently develop into a warm event [see more discussion of the model
398 processes in Deser et al. (2012)].

399 Figure 7 further compares the corresponding wavelet analysis of PC1 and PC2. The left
400 panel represents the wavelet power spectrum and the right panel indicates the global power
401 spectrum averaged over the two time series. High variability is represented by red, whereas blue
402 indicates a weak variability in the wavelet power spectrum. The observation shows that the
403 nonstationary variability of PC1 and PC2 changes with time at multiple time scales. The global
404 power spectrum indicates peaks at about 5 and 12 years. The dashed lines show the 95%

405 significance level and only the 5-year peak passes the significance test. However, both peaks are
406 consistent with the wavelet analysis of Niño3.4 index in Tzeng et al. (2012). This further
407 supports the notion that PC1 reflects the change in ENSO. In the wavelet of PC2, the global
408 power spectrum in the interannual variability range is quite similar to the wavelet of PC1 with a
409 weaker spectrum, which is clearly the precursor of PC1. The other peak of 12 years (11.7 years,
410 precisely) can be seen in both PC1 and PC2, but both do not pass the significance tests in the
411 observation due to the short observation record (1957–2010). The CESM provides a useful tool
412 to further investigate this since we can run the model for a longer period. The control simulation
413 shows quite a clear peak of about 5 years in PC1 and a peak of about 12 years in PC2. This
414 supports the view of Furtado et al. (2012) that PC1 dominates at the interannual scale of ENSO
415 variability while PC2 relates more to the decadal or low-frequency variability assuming the
416 underlying Pacific dynamics and variability can be well represented in the model physics. Indeed,
417 a larger change can be seen from the power spectrums in the model comparisons. The decadal
418 variability in the PC2 of both the $Wind_{clim}$ and SST_{clim} experiments is significantly suppressed
419 (Fig. 7). On the other hand, the interannual variability mode of PC2 is enhanced. No significant
420 change in the power spectrum can be found in PC1 (apart from perhaps a weak enhancement at
421 the interannual scale of variability). These results show that the IPWP does indeed modify a
422 particular pathway related to the decadal variability in the model.

423 But what is that pathway, in order that it alters the variability related to CEOF2 (and its
424 corresponding PC2), and how does this pathway relate to previous studies? Figure 8 further
425 shows the correlation maps between the December–February (DJF) PC2 and SST anomalies for
426 DJF and several lead times (MAM, JJA, SON, and DJF+1) based on the observation and the
427 CESM simulations. We find the evolved patterns in Fig. 8 are very similar to those in Fig. 1 in

all panels and the correlation map of the detrended WNP index defined by Wang et al. (2012) with the same seasonality. Strong correlations are evident near the East Asian coastline, which extend further eastward along the KE in the early stages and shift equatorward in later seasons. Comparing the panel for the observation with Fig. 1, the WNP SST anomalies indeed show evolution typical of the VM/MM mode, which is associated with the SST footprint of the NPO (Fig. 5). The correlation maps at different lead times show how the NPO (i.e., CEOF2) induces changes in surface heat fluxes in the central-eastern North Pacific, which generate a meridional tripole pattern of the VM/MM (Vimont et al. 2003; Alexander et al. 2010; Yu and Kim 2011; Ding et al. 2014a). Ding et al. (2014a) suggest that this tripole SST pattern in the North Pacific acts as an effective pathway for NPO-like atmospheric variability to drive EM variability (warming in the central Pacific particularly) via the SFM [see Ding et al. (2014a) for the detailed dynamical processes]. It is important to point out that the evolved patterns involve not only the central-eastern North Pacific, described comprehensively in the literature, but also the change of the WNP.

The CESM control simulation shows similar but slightly different patterns of evolution. We can still see the typical evolution of the SFM triggering EM (Alexander et al. 2010). However, the $Wind_{clim}$ and SST_{clim} experiments seem to have broken the teleconnection in the eastern Pacific SST anomalies. The northeast SST footprint almost disappears after SON and DJF+1 in both the $Wind_{clim}$ and SST_{clim} experiments. Note that the tropical response still exists without significant changes. The comparison confirms that removing the O–A in the IPWP region may significantly affect the tropical–extratropical teleconnection. In the next section, we detail the origin of the low SST anomalies of the WNP one year ahead of El Niño resulting from the IPWP variability.

4. Origin of the ENSO precursor resulting from the basin-scale tropical–extratropical teleconnection

Many previous studies have addressed the potential influence of the NPO on ENSO. However, not many people understand exactly how the NPO modulates ENSO, particularly EM, because the underlying dynamics are still not clear. Most relevant works emphasize the dynamics of the SFM. Pegion and Alexander (2013) indicated that the existence of negative (positive) NPO in winter(0) does not always result in El Niño (La Niña) the following winter [winter(1)]. Some studies have also shown that the impact of the NPO on the development of ENSO conditions through the SFM relies on the state of the tropical Pacific (e.g., Anderson 2007; Alexander et al. 2010). Anderson (2007) found that the link between the SLP anomalies associated with winter(0) NPO and ENSO-related SST anomalies in winter(1) is stronger when the positive heat content anomalies in the western equatorial Pacific occur in autumn(−1), followed be negative SLP anomalies over the subtropical central North Pacific in D(−1)JF(0). A weak relation exists between the winter SLP anomalies and the ENSO state in the following year when the above two patterns are of the same sign. Both heat content and subtropical SLP states are related, but the variability of the subtropical SLP anomalies affects the occurrence of El Niño more one year later. His results indicate that a deeper (shallower) thermocline in the western equatorial Pacific together with a negative (positive) NPO is more effective in producing warm (cold) ENSO events, but no specific reason was given.

Here, we propose two effective pathways along which the atmospheric and oceanic dynamics in the IPWP can affect ENSO evolution. One pathway is associated with the tropical recharge–oscillator mechanism (Chen et al. 2014) and the ocean channel (Yuan et al., 2011, 2013). This pathway can potentially explain the triggering role of the heat content discussed in

474 Anderson (2004, 2007) and how it is related to ENSO evolution in previous studies (e.g., Meinen
475 and McPhaden, 2000). The other pathway is detailed here to describe how the IPWP variability
476 modulates the strength of the NPO, which may affect the strength of El Niño in the subsequent
477 year. We first focus on the WNP domain, where a strong precursor signal occurs approximately
478 one year in advance (Fig. 1). Over the extratropical North Pacific, the Kuroshio–Oyashio
479 extension (KOE) region is a key region where the oceanic variability can significantly impact the
480 atmosphere (Li and Wu 2013; Frankignoul et al. 2011). After separating from the eastern coast
481 of Japan, the Kuroshio carries more than 100 Sv of warm water eastward into the central North
482 Pacific. As the cold dry air from the Eurasian continent meets the warm Kuroshio water, a large
483 amount of heat and moisture is extracted from the surface, resulting in strong convection in the
484 atmospheric and oceanic boundary layers, and leading intensive rainfall over the KOE region.
485 Frankignoul et al. (2011) found that the meridional shifts of the Oyashio Extension (OE) and KE
486 can affect the atmospheric circulation over the Pacific. In particular, they found the barotropic
487 response to the meridional shifts of the OE front resembles the NPO/Western Pacific (WP)
488 pattern variability. A northward frontal displacement of the OE causes a positive phase of the
489 NPO/WP at a lag of 2 months. The KE front has a similar impact but the amplitude is smaller
490 than the OE front. We follow a similar approach and define a meridional gradient of SST from
491 November to May because the extratropical SST variability is large near the strong SST
492 gradients along the oceanic fronts associated with the Kuroshio/Oyashio and its extension when
493 the ocean circulation changes are effective in influencing the SST (Qiu 2002; Vivier et al. 2002;
494 Schneider et al. 2002). Figure 9 shows the averaged negative meridional gradient of the original
495 SST *(−dSST/dy*, without any smoothing) during November–May in the (a) observation and (b)
496 CESM control simulation. A strong meridional SST gradient can be found between the Kuroshio

497 and Oyashio fronts (KOE region) in both the observation and CESM simulation. Note that the
498 axes of OE and KE shift slightly northward in the CESM control simulation compared with the
499 observation due to its coarse model resolution. Therefore, the latitudes of the maximum SST
500 gradient are also shifted accordingly.

501 In the observation, there is another large SST gradient band south of the KE between 20°N
502 and 30°N, extending from the East China Sea to the central Pacific. This band is seen in the
503 CESM control simulation as well. We superimpose the CEOF2 SST anomalies from Fig. 5
504 (dashed contours in Fig. 9) on the SST gradient fields. It is interesting to see that this band
505 closely matches the CEOF2 pattern of largest variability. This band is also similar to the
506 northeastward-elongated evolution path in Fig. 1 as the maximum correlation of Niño4 develops
507 with time. We suspect this strong SST gradient band is associated with the VM/MM mode
508 resulting from the NPO/WP forcing, which can substantially affect the eddy fields in the STCC
509 region (Qiu and Chen 2010; Shen et al. 2014). Further analysis indicates that this band is not
510 seen in the summer and fall seasons; rather, it develops during the winter and extends into spring.
511 These consistencies imply an intensive O–A interaction in the North Pacific at different scales.

512 Figure 9 leads us to further investigate the strong meridional SST gradient *(−dSST/dy)*
513 variability in a region of the WNP (30°–40°N, 160°–220°E) and how this variability affects the
514 NPO variability relating to ENSO evolution. The chosen region is located just downstream of the
515 KOE between the two regions of maximum SST gradient where a turning pattern likely forms. In
516 the KOE region, the surface wind flowing over a large meridional gradient of SST can lead to
517 large changes in boundary layer stability, surface wind stress, as well as latent and sensible heat
518 fluxes (Small et al., 2008). Figure 10 shows the time series of meridional SST gradient
519 *(−dSST/dy)* variability averaged in the region defined by this box in the (a) observation and (b)

CESM control simulation. The PC2 of CEOF2 in Fig. 5 is also superimposed for comparison. Both time series are very similar, except more local variability and seasonality can be seen in the KOE meridional SST gradient variability. Specifically, the time series of the meridional SST gradient has a marginal correlation of 0.41 with PC2 at a 1-month lead time in the observation. Similar behavior can be found in the CESM control simulation. These results support our speculation that the Kuroshio SST variability plays a role in controlling the CEOF2 pattern in the North Pacific.

We next perform composite analyses for the SLP anomalies when the amplitude of the associated meridional SST gradient exceeds ranges of 1 standard deviation (std) in the observation and CESM simulations (shown as dashed lines in Fig. 10). Figure 11 shows the composites of SLP anomalies from November to May (NDJFMAM) at different lag times (ranging from SLP leading by 3 months to SLP lagging by 4 months) for the positive phase of the meridional SST gradient *(−dSST/dy)* (amplitude is greater than 1 std in Fig. 10). The NPO patterns are also superimposed for reference. A northward shifting and intensity change of the SLP composite can be observed from the lag sequence in Fig. 11 during the positive phase of the meridional SST gradient. We find that the two centers of the composite of the SLP dipole are collocated with the NPO's centers of action (contours) when the SLP anomalies lag the meridional SST gradient by roughly 2 months in the observation (left panel). The southern lobe of the SLP dipole is also strengthened over time, while the northern lobe is weakened. This indicates the change of meridional SST gradient in the KOE region (Fig. 10) can lead to the positive NPO-like SLP patterns 2 months after the meridional SST gradient in the KOE reaches its maxima. A similar collocation of the SLP composite with NPO centers of action can be found in the CESM experiments with roughly the same lag time. The northward shifting of the SLP

543 composite is also evident as the southern lobe is strengthened.

544 However, if we focus on the two sensitivity experiments, the southern lobe strengths of the
545 SLP dipoles in the $Wind_{clim}$ and SST_{clim} experiments are more than two times weaker than those
546 in the CESM control experiment. The northern lobe strengths are unlikely to change compared
547 with the CESM control experiment. Furthermore, the phase of SST_{clim} seems to be slightly
548 different. The southern center of the SLP dipole in the $Wind_{clim}$ experiment shifts eastward and
549 does not collocate with the NPO centers (black contours), unlike the CESM control simulation.
550 We can also see a largely weakened NPO-like development (particularly the southern lobe) in
551 the $Wind_{clim}$ experiment and a slightly weakened development in the SST_{clim} experiment. These
552 results are consistent and indicate the two sensitivity experiments indeed modulate the NPO
553 through the modulation of SLP anomalies from the change of meridional SST gradient in the
554 KOE region.

555 The same phenomena with exactly the opposite sign of the SLP composite can be seen when
556 we examine the negative phase of the meridional SST gradient (see Fig. 12 for the same
557 composite plot but with amplitude less than −1 std). The negative NPO-like dipole also evolves
558 and develops with different magnitude. The southern lobes are strengthened, while the northern
559 lobes are weakened. The lag of the SLP composite collocated with the NPO dipole is also
560 roughly 2–3 months in both the observation and CESM control simulation. These signals are
561 evident at the strengthened southern lobe.

562 A similar eastward shifting of SLP anomalies and their decoupling with the NPO's center
563 can be found in the $Wind_{clim}$ and SST_{clim} experiments. The northern lobe of the SLP anomalies is
564 relatively weak. In the SST_{clim} experiment especially, the southern lobe is stronger than the
565 control simulation and is dominant. Since the evolving patterns are asymmetrical, we do not take

566 the composite difference between the opposite phases to emphasize the different evolutions of
567 SLP anomalies. This difference in the opposite meridional SST gradient is also consistent with
568 the asymmetrical evolution pattern of El Niño and La Niña. The negative phase of the meridional
569 SST gradient composite enhances the negative phase of the NPO-like SLP anomalies.
570 Furthermore, the resulting negative NPO-like dipole can strengthen the subtropical westerly
571 anomalies, leading to the consequential SFM, which has been addressed extensively in previous
572 studies (e.g., Alexander et al., 2010; Ding et al., 2014a).

573 Figure 13 further examines the corresponding composites of surface latent heat flux (major
574 source of the total heat exchange at the surface) and surface wind vectors for the negative phase
575 of the meridional SST gradient. The reverse set of processes occurs during the positive phase and
576 is not shown to simplify the discussion. In the observed negative phase of the meridional SST
577 gradient (left panel), the latent heat flux shows a large amount of heat loss to the atmosphere
578 (positive upward) in the subtropical WNP before the SLP composites are collocated with the
579 NPO centers of actions at a lag of 2 months. The pattern is similar to the general latent heat
580 release in the WNP which cools the ocean surface. The follow-up weakening and shrinking of
581 the latent heat flux after the lag of 2 months is then consistent with the enhancement of the
582 negative SST anomalies due to the formation of the VM/MM mode. In the central-eastern
583 subtropical Pacific, typical negative latent heat flux anomalies (downward to the ocean)
584 associated with SFM can also be seen at a lead of 3 months, and decay with time. The resulting
585 net latent heat flux exchanges in the Pacific are combined with the anomalous surface westerly in
586 the central-eastern tropical Pacific, thereby warming the tropical SST. The associated Pacific
587 dynamics are consistent with the characteristics of the evolved SFM (Vimont et al. 2009;
588 Alexander et al. 2010). The CESM control simulation also shows a similar but stronger pattern

589 than the observation. The time-lag is also slightly different. This confirms the CESM control
590 simulation can successfully simulate the dynamical process associated with the ENSO precursor
591 pathway (Alexander et al. 2010; Deser et al. 2012). However, in the $Wind_{clim}$ experiment, the
592 negative latent heat flux in the eastern Pacific is significantly weaker than that in the CESM
593 control simulation, while the latent heat flux pattern in the SST_{clim} simulation is in the middle.
594 There is almost no associated heat gain of the ocean in the central-eastern subtropical Pacific in
595 the $Wind_{clim}$ experiment after the lag of one month. This can also explain the reduced
596 extratropical forcing in the correlation map of Fig. 8. In the SST_{clim} experiment, the heat flux
597 response still exists; however, the pattern differs from the observation and the CESM control
598 simulation due to the change of surface wind anomalies.

599 These results of the negative phase of the meridional SST gradient suggest the Kuroshio
600 SST variability may modulate the variability of the NPO through a strengthened negative
601 NPO-like SLP pattern. More precisely, the meridional SST gradient in the KOE region plays a
602 triggering role. Figure 14 shows the composites of vertical velocity Ω (negative upward and
603 positive downward) and streamlines for the same negative phase of the meridional SST gradient
604 shown in Fig. 13 along the vertical section averaged between 30°N and 45°N. Note that the
605 vertical velocity in the streamline is normalized by -1000 in order to be comparable with
606 horizontal velocity scale with positive upward. In the KE region east of Japan, we can see an
607 upward tendency approximately between 150°E and 180°E in associated with a downward
608 enhancement at its east in the observation. The downward enhancement results from the
609 enhanced negative NPO pattern shown in Fig. 12. A similar vertical structure can be seen in the
610 CESM control simulation east of Japan, where the velocity is upward at west of 160°E and
611 downward at east of 160°E. However, the upward motion appears to be blocked in the mid

612 troposphere in the $Wind_{clim}$ and SST_{clim} experiments. These patterns are consistent with the
613 surface latent heat flux pattern in Fig. 13.

614 We further confirm that the associated pathway modifies the NPO through the well-known
615 enhanced Hadley circulation (atmospheric bridge) by plotting the other meridional section above
616 the Kuroshio region. Figure 15 show the corresponding composites of vertical velocity Ω and
617 streamlines as Fig. 14 along the vertical section averaged between 120°E and 150°E. The vertical
618 velocity in the streamline is normalized by -200 in order to be comparable with horizontal
619 velocity scale with positive upward. All observation and model results show the enhanced and
620 then decayed Hadley circulation in the lag sequence. However, the lag time may be slightly
621 different. In general, the teleconnection propagates from the subtropical surface to the
622 mid-latitude high levels, and then back to the surface causing the VM/MM patterns through the
623 enhanced Hadley circulation. The lag sequences from top to bottom confirm the vertical motion
624 combined with the intensive air–sea interaction occurs along the Kuroshio and its gyre
625 circulation in the WNP. We call this the Kuroshio pathway. From several other meridional
626 sections averaged from different longitudes, we also find the teleconnection move from west to
627 east (not shown here) similar to the zonal migration in Fig. 14. The northeastward band observed
628 in the surface EOF2 pattern is actually the footprint of the associated atmospheric propagation
629 through the Hadley circulation with the aid of the SFM. The positive composites show a reduced
630 Hadley circulation, while the negative composites show an enhanced Hadley circulation. In
631 addition, the Kuroshio pathway is also tilted from west to east. The relevant tropical–
632 extratropical teleconnection involves not only the meridional circulation, but also the zonal
633 change. In the $Wind_{clim}$ and SST_{clim} experiments, the patterns are similar to those in the CESM
634 control simulation, but the strengths are different in some stages because the variability resulting

635 from the IPWP forcing is reduced.

636 In summary, Figure 12 shows the negative NPO-like phase intensifies with time and reaches
637 the maximum at no lag in association with the negative phase of the meridional SST gradient
638 variability in the KOE region. The SLP dipoles also shift northward with time and migrate to the
639 NPO center of action at a lag of around 2 months of the negative meridional SST gradient phase.
640 Cyclonic anomalous winds are also observed in the mid-latitudes (Fig. 13) and reduce the
641 easterly trade winds in the tropics. The lag sequences shows a significant reduction of upward
642 latent heat flux after a 2 month lag in the WNP along the Kuroshio and its gyre circulation. At
643 the same time, downward latent heat flux can be observed in the central-eastern subtropical
644 Pacific, but the magnitudes gradually decay with time. These results are consistent with the
645 evolution of the SFM and its resulting VM/MM pattern. Figure 15 further confirms the change of
646 Hadley circulation and the associated teleconnection. Based on these, we can conclude that the
647 pattern in the WNP is changed in associated with the change of Hadley circulation, Kuroshio
648 SST variability can enhance the NPO variability, and a negative NPO-like pattern favors the
649 generation of the SFM and thus warming in the central-eastern Pacific. The vertical section
650 sequence along the Kuroshio pathway shows the upper-troposphere convection may play an
651 important role in modulating the teleconnection pattern and may directly result from
652 off-equatorial Rossby wave propagation.

653 Furthermore, all relevant fields in the $Wind_{clim}$ experiment generally show an extensively
654 weaker response than the CESM control simulation. The SLP dipole anomalies associated with
655 the negative SST in the WNP also weaken in the $Wind_{clim}$ experiment. Thus, the Kuroshio
656 pathway modulating the NPO is also weakened because of the shutdown of the IPWP variability.
657 Also, the delayed 2-month lag of the atmospheric response resulting from surface flux change in

658 the WNP is similar to the atmospheric response of the OE and KE discussed in Frankignoul et al.
659 (2011), which may also affect the variability of the NPO. This discussed in more detail in the
660 next section.

661 **5. Discussion**

662 Past studies on the NPO have focused mainly on the impacts of its teleconnection patterns
663 on the weather and climate of North America (Linkin and Nigam 2008) and how the NPO
664 initiates ENSO through the SFM. Most studies looking at the NPO-induced SFM focus on the
665 consequent changes of surface and subsurface heat content in the central-eastern tropical Pacific
666 (e.g., Anderson 2004; Anderson and Maloney 2006; Anderson 2007). The Kuroshio pathway we
667 describe here mostly affects the NPO's southern center of the action (north of Hawaii) prior to
668 the NPO-induced SFM. This is similar to the finding of low-frequency forcing of EM in
669 modulating the low-frequency mode of the NPO in Di Lorenzo et al. (2010) and Furtado et al.
670 (2012). However, we point out a more direct impact of the IPWP variability in modulating the
671 NPO. This explains all northern hemispheric precursors of El Niño in the literature and helps us
672 to form a framework of ENSO prediction and an integrated Pacific climate paradigm.

673 Our results show that the IPWP O–A variability can be seen as the trigger-forcing of the
674 tropical–extratropical teleconnection associated with the CEOF2 in terms of ENSO evolution.
675 The heat-forcing in the IPWP triggers off-equatorial propagation along the Kuroshio, which
676 modulates the variability of the NPO. Note that this Kuroshio pathway is one particular pathway
677 in the northern hemisphere subject to IPWP heating; another pathway exists in the southern
678 hemisphere (Ding et al. 2014b). These off-equatorial atmospheric responses resemble the
679 so-called Gill-type response (Gill 1980) in the tropics. In the Gill model (Gill 1980; Philander et
680 al. 1984; Hirst 1986), the latent heating of the atmosphere (i.e., cumulus heating of the middle

and upper troposphere) drives low-level winds proportional to SST anomalies (Hirst 1986) or related to surface heat flux anomalies (Zebiak 1982) in both hemispheres, consistent with the observed heat flux changes shown here. The air rising in the upper troposphere may eventually diverge, and the divergence region acts as a source of planetary Rossby waves in the upper troposphere that propagate into the mid-latitudes as a series of wavetrains (Trenberth et al. 1998). Our results confirm that the IPWP region is one origin of these wavetrains.

The NPO is commonly defined by a north/south dipole centered over Alaska and Hawaii (Fig. 5). Furtado et al. (2012) found that the southern lobe of the NPO (over Hawaii) contains significant power at low frequencies (7–10 years), while the northern lobe (over Alaska) has no dominant frequencies. They also showed that the low-frequency variations (period >7 years) of the NPO (particularly its southern lobe) is linked with the SST anomalies variability associated with the change of EM in the central tropical Pacific. They suspected the underlying mechanism may link to the Rossby wavetrains originated in the central tropical Pacific. However, the picture may not be so simple. If the origin is the central tropical Pacific, why does the largest regression occur in the extratropical North Pacific rather than the central tropical Pacific (Fig. 9 in Furtado et al. 2012)? Our results suggest that the IPWP is the dominant tropical origin in modulating the NPO through the Kuroshio pathway in which the strong divergence (convergence) at the southern lobe of the NPO forces the wavetrains. Mehta and Fayos (2005) also found that the decadal to multi-decadal scale IPWP variability can modulate the interannual variability of ENSO. This view is further supported by the wavelet spectrum in the $Wind_{clim}$ and SST_{clim} experiments, where the decadal spectrum peaks are significantly reduced compared with the prominent decadal spectrum peak in the CESM control simulation. We suspect the diminishing of the decadal spectrum peak may be associated with the reduction of Hadley circulation

704 (meridional variability of the NPO location) and surface heat flux. In the two sensitivity
705 experiments, the larger change occurs at the southern lobe of the NPO and is consistent with the
706 weakening of the dominant spectrum peak. We further examined the circulation pattern along the
707 vertical section of 200°E and found no direct evidence of the propagating process from the
708 central tropical Pacific (not shown). Thus, the northeastward propagating Kuroshio pathway may
709 be the pivotal route controlling the low-frequency (decadal) variability of the second dominant
710 mode of North Pacific climate variability. Note that there is another pressure low in the WNP of
711 CEOF2 [also found in Anderson (2004, 2007)]. A more detailed and careful study is required to
712 clarify the role of this pattern and the associated dynamics. It is possible that EM may change the
713 air–sea interaction in the western tropical Pacific and the IPWP.

714 The present study supports a specific view that the dominant stochastic forcing for ENSO
715 comes from the thermodynamic heating source in the IPWP. Removing the IPWP variability in
716 the $Wind_{clim}$ and SST_{clim} experiments reduces the physical instability of the associated O–A
717 interaction. However, the IPWP region is still as warm as usual, so the tropical ENSO dynamics
718 are still active in the sensitivity experiments. Therefore, there is no significant change in the
719 wavelet analysis of the associated PC1. Our result can further explain the finding of all previous
720 ENSO precursors observed 12–18 months ahead. For example, the negative IOD in year(−1)
721 introduces a warmer than normal temperature in the IPWP (Izumo et al. 2010). This can easily
722 enhance the local heating source and trigger the thermodynamic instability in the IPWP region.
723 Also, the large heat content found in the western equatorial tropics in year(−1) (e.g., Meinen and
724 McPhaden 2000; Anderson 2007; Chen et al. 2014) triggers the Gill-type response and is
725 fundamental for the dynamics of ENSO in the tropics. This further confirms that the ENSO
726 evolution related to the IPWP heating source may have a remote impact on the North Pacific

727 climate in which the deeper ocean dynamics and local air–sea interaction are more confined in
728 the tropics with a slower response, while the atmospheric response associated with shallow
729 boundary layers can propagate faster off-equatorially to the extratropical regions. Based on the
730 current setup, the canonical ENSO (corresponding to CEOF1) in these two experiments cannot
731 be changed significantly because the recharge–discharge mechanism is still valid and we only
732 reduce the variability, which is vital to the tropical–extratropical teleconnection (CEOF2).

733 There are also some other potential mechanisms that could excite the thermodynamic
734 heating source in the IPWP. For example, the East Asian summer monsoon may affect the ENSO
735 variability (Li et al. 2007). Chang et al. (2009) also found that significant negative (positive) SST
736 anomalies in the IPWP region appear in the strong (weak) Subtropical Mode Water (STMW)
737 case. Their statistical analysis indicated that summer(−1) STMW variability can also affect
738 ENSO events 18 months later. They suspected that summer STMW(−1) variability produces
739 subtropical atmospheric variability through long-term persistent SST anomalies over its
740 reemergence area to derive the VM pattern, and eventually modulates the amplitude of ENSO
741 events. But the role of the STMW still requires further clarification.

742 Although the atmospheric response is essential for the Kuroshio pathway described here, the
743 existence of Kuroshio is very important to guide it and the subsequent VM/MM responses. Liu
744 and Wu (2004) assessed the role of O–A coupling in the atmospheric response to variability in
745 the KOE SST and suggested that ocean dynamics are important for the influence of SST
746 anomalies in the KOE region on atmospheric circulation. Our results further confirm that the
747 enhancement of the regional air–sea interaction along the fronts of Kuroshio and its downstream
748 extension changes the Hadley circulation through the change of surface heat flux. Most
749 important of all, this pathway ties directly to ENSO evolution one year in advance. Our results

750 are in fact consistent with previous evidence of Kuroshio's influence on the NPO reported by
751 Hirose et al. (2009). They also showed that changes in the Tsushima Warm Current (a current
752 fed by the Kuroshio, which passes between Korea and Japan) during autumn were correlated
753 with the following winter NPO/WP pattern. Moreover, the consequent response of atmospheric
754 circulation to the Kuroshio can also be found through a positive feedback process in the WNP
755 (Qiu and Chen, 2010; Shen et al. 2014). The intensive coupled O–A interaction in the WNP
756 significantly modulates the North Pacific climate variability.

757 The Kuroshio pathway associated with the atmospheric patterns does not conflict with the
758 existence of traditional tropical ENSO theories, such as the delay–oscillator mechanism and the
759 recharge–discharge mechanism. The tropical dynamic pathway for ENSO development has been
760 studied extensively. In general, the ENSO relevant impacts resulting from the IPWP variability
761 may evolve globally. The atmospheric pathway associated with Kuroshio is only one part of the
762 complete picture of ENSO evolution. However, different time scales among these pathways and
763 processes result in the so-called ENSO precursor because the atmospheric processes are often
764 faster than the tropical ocean dynamics. Several recent studies have suggested that the IOD's
765 influence is achieved through a modification of the Walker circulation branches over the western
766 Pacific and the nearby circulation (Li et al. 2003; Annamalai et al. 2005; Kug and Kang 2006;
767 Luo et al. 2008), prolonging the lead time for ENSO prediction for up to 14 months before they
768 peak (Izumo et al. 2010). The delayed (Suarez and Schopf 1988; Battisti and Hirst 1989) and
769 advective–reflective oscillators (Picaut et al. 1997) can act to reinforce the Pacific response to
770 the heating source of the IPWP, and drive eastward current anomalies and positive SST
771 anomalies in the central Pacific through zonal advection of the warm pool eastern edge [the main
772 process that controls SST variations in the central Pacific, e.g., Vialard et al. (2001)]. All of these

studies point to the pivotal role of the IPWP variability in ENSO evolution. Moreover, the preconditioned WWV in the recharge–discharge mechanism reflects the associated oceanic responses and the subsurface changes to precondition the Pacific WWV [as do westerly wind bursts, e.g., Fedorov (2002)]. The resulting SST anomalies in spring(0) are amplified by the Bjerknes feedback and evolve into an El Niño event at the end of the year. Therefore, the IPWP region may be the only hot spot that can explain not only the tropical ENSO evolution, but also the extratropical modulation of ENSO through the Kuroshio pathway.

6. Conclusion and future directions

The origin of the well-known extratropical forcing on ENSO and its associated pathway originating from the WNP has been analyzed in this study using observations and the CESM. The two dominant modes of surface variability can explain most of the North Pacific climate variability in both the observation and CESM and are related with each other. CEOF1 represents the ENSO/PDO variability, which expresses the zonal variability in the tropics and mid-latitudes. CEOF2 shows the NPO/VM variability reflecting the footprint of the meridional variability through the tropical–extratropical teleconnection. We also found that CEOF1 is dominated by the variability at the interannual scale, while CEOF2 is dominated by decadal-scale variability. CEOF2 can be considered as the precursor signal of El Niño through the identified Kuroshio pathway affecting the NPO, and thus the VM/MM (Fig. 16).

These results lead us to believe that the IPWP region is a hot spot where the O–A perturbation resulting from different causes can trigger ENSO events one year later, and the O–A interaction can precondition both the atmospheric and subsurface ocean structures, thereby allowing the relevant ENSO onset mechanisms to occur stochastically. The O–A interaction in the IPWP region also allows the recharge–oscillator mechanisms to reinforce by the instability of

796 the IPWP and trigger the El Niño precursor. The Kuroshio pathway related to the El Niño
797 precursor is not new and can be used to clarify some questions in Anderson (2004, 2007), who
798 found a similar anomalous pressure and subsurface heat content pattern in the WNP. Here, we
799 further confirm its origin being the IPWP region using the CESM sensitivity experiments. Many
800 possible heating sources can excite the O–A interaction in the IPWP, meaning it is difficult to
801 distinguish these sources in reality. The Kuroshio pathway modifies the NPO, and thus affects El
802 Niño, while the associated atmospheric dynamics are different from the tropical ENSO dynamics.
803 However, they can serve as precursors because the signals propagate faster than the subsurface
804 ocean transport in the tropical ENSO dynamics.

805 The detailed O–A interaction involved in the WNP is still not clear, and we confirm a
806 similar thermodynamically coupled wind–evaporation–SST feedback (Xie and Philander 1994;
807 Vimont et al. 2009; Alexander et al. 2010) for the SFM, and thus the VM/MM, may be applied.
808 Vimont (2010) provided a dynamical explanation for this thermodynamically coupled variation
809 in the tropics. Previous studies also confirm that the SFM may effectively trigger El Niño when
810 the NPO occurs in combination with La Niña-like SST during the winter (Anderson 2007;
811 Alexander et al. 2010; Vimont 2010), which is consistent with the assumption that the large heat
812 content triggers the thermodynamic instability in the IPWP. Moreover, the IPWP region is also
813 an area where deep convection influences the ascending branch of the Walker circulation, and is
814 potentially a particular driver for the Hadley circulation. Further investigations into the relevant
815 air–sea interaction in the WNP are planned.

816 The diminishing of the decadal variability of CEOF2 in the $Wind_{clim}$ and SST_{clim}
817 experiments is also not clear at this stage. All of the dynamical processes discussed here are
818 seasonal atmospheric or surface processes directly related to the modulation of the NPO on

819 subsequent ENSO events. However, our wavelet analysis suggests the Kuroshio pathway can
820 directly link to the low-frequency variability of North Pacific climate. We found changes of the
821 NPO in strength and location, which may potentially modify the extratropical ocean variability.
822 This suggests a potential role of North Pacific ocean dynamics in the North Pacific decadal
823 variability. The extratropical atmosphere/ocean interaction may generate or excite the
824 decadal-scale tropical Pacific variability through subduction (e.g., Gu and Philander, 1997).
825 Further analysis of the sub-surface ocean dynamics is required.

826 Note that the Kuroshio pathway associated with the sequential SFM described here can be
827 viewed as one dominant pathway in the northern hemisphere, which can explain many northern
828 hemispheric ENSO precursors in the literature. Alexander et al. (2010) tested the SFM
829 hypothesis by imposing the NPO-related surface heat flux anomaly forcing in a coupled general
830 circulation model, and their results showed that the El Niño-like warming was generated in ~70%
831 of ensemble simulations. Our results confirm that the major ENSO cycle is still determined by its
832 relevant tropical subsurface dynamics (Chen et al. 2014). The Kuroshio pathway is only one part
833 of the O–A interaction triggered in the IPWP region. The ocean dynamics pathway related
834 directly to the ENSO cycle will be further discussed in a separate paper.
835

836 **REFERENCES**

837 Alexander MA, Vimont DJ, Chang P, Scott JD (2010) The impact of extratropical atmospheric
838 variability on ENSO: Testing the seasonal footprinting mechanism using coupled model
839 experiments. J Clim 23:2885–2901

840 Anderson BT, Maloney E (2006) Interannual tropical Pacific sea surface temperatures and their
841 relation to preceding sea level pressures in the NCAR CCSM2. J Clim19:998–1012

842 Anderson BT (2004) Investigation of a large-scale mode of ocean–atmosphere variability and its
843 relation to tropical Pacific sea surface temperature anomalies. J Clim 17:4089–4098

844 Anderson BT (2007) On the joint role of subtropical atmospheric variability and equatorial
845 subsurface heat content anomalies in initiating the onset of ENSO Events. J Clim 20:1593–1599

846 Annamalai H, Liu P, Xie SP (2005) Southwest Indian Ocean SST variability: Its local effect and
847 remote influence on Asian Monsoons. J Clim 18:4150–4167

848 Ashok K, Behera SK, Rao SA, Weng H, Yamagata T (2007) El Niño Modoki and its possible
849 teleconnection. J Geophys Res 112:C11007. doi:10.1029/2006JC003798

850 Battisti DS (1988) The dynamics and thermodynamics of a warming event in a coupled tropical
851 atmosphere/ocean model. J Atmos Sci 45:2889–2919

852 Battisti DS, Hirst AC (1989) Interannual variability in the tropical atmosphere/ocean system:
853 Influence of the basic state and ocean geometry. J Atmos Sci 46:1687–1712

854 Bjerknes J (1969) Atmospheric teleconnections from the equatorial Pacific. Mon Wea Rev
855 97:163–172

856 Bond NA, Overland JE, Spillane M, Stabeno P (2003) Recent shifts in the state of the North
857 Pacific. Geophys Res Lett 30:2183. doi:10.1029/2003GL018597

858 Chang P, Zhang L, Saravanan R, Vimont DJ, Chiang JCH, Ji L, Seidel H, Tippett MK (2007)
859 Pacific meridional mode and El Niño-Southern Oscillation. Geophys Res Lett 34:L16608.
860 doi:10.1029/2007GL030302

861 Chang R, Zhang QY, Li RF (2009) North Pacific premonitory sign of the ENSO event. Geophys
862 Res Lett 36:L03818. doi:10.1029/2008GL036597

863 Chen HC, Sui CH, Tseng YH, Huang BH (2014) An analysis of climate oscillations in Pacific
864 subtropical cells. submitted to Clim Dyn.

865 Chiang JCH, Vimont DJ (2004) Analogous Pacific and Atlantic meridional modes of tropical
866 atmosphere-ocean variability. J Clim 17:4143-4158

867 Clement AC, Seager R, Murtugudde R (2005) Why are there tropical warm pools? J Clim
868 18:5294–5311

869 Danabasoglu G, and Coauthors (2012) The CCSM4 ocean component. JClim 25:1361–1389

870 Deser C, and Coauthors (2012) ENSO and Pacific decadal variability in the Community Climate
871 System Model version 4. J Clim 25:2622–2651

872 Di Lorenzo E, Schneider N, Cobb KM, Franks PJS, Chhak K, Miller AJ, McWilliams JC, Bograd
873 SJ, Arango H, Curchitser E, Powell TM, and Rivière P (2008) North Pacific Gyre Oscillation links
874 ocean climate and ecosystem change, Geophys Res Lett, 35, L08607,
875 doi:10.1029/2007GL032838.

876 Di Lorenzo E, and Coauthors (2010) Central Pacific El Niño and decadal climate change in the
877 North Pacific. Nature Geosci 3:762–765

878 Ding R, Li J, Tseng YH, Sun C (2014a) The Victoria mode in the North Pacific linking
879 extratropical SLP variations to El Niño Modoki. submitted to J Geophys Res.

880 Ding R, Li J, Tseng YH (2014b) The impact of south Pacific extratropical forcing on El Niño and
881 comparisons with the North Pacific. submitted to Clim Dyn.

882 Fedorov AV (2002) The response of the coupled tropical ocean-atmosphere to westerly wind
883 bursts. Q J Roy Meteorol Soc 128:1–23

884 Frankignoul C, Sennéchael N, Kwon YO, Alexander MA (2011) Influence of the meridional
885 shifts of the Kuroshio and the Oyashio Extensions on the atmospheric circulation. J Clim
886 24:762–777

887 Fu R, Del Genio AD, Rossow WB (1994) Influence of ocean surface conditions on atmospheric
888 vertical thermodynamic structure and deep convection. J Clim 7:1092–1108

889 Furtado JC, Di Lorenzo E, Anderson BT, Schneider N (2012) Linkages between the North
890 Pacific Oscillation and central tropical Pacific SSTs at low frequencies. Clim Dyn 39:2833–2846

891 Gent PR, and Coauthors (2011) The Community Climate System Model version 4. J Clim 24:
892 4973–4991

893 Gill AE (1980) Some simple solutions for heat-induced tropical circulation. Quart J Roy Meteor
894 Soc 106:447–462

895 Gu D, Philander SGH (1997) Interdecadal climate fluctuations that depend on exchanges between
896 the tropics and extratropics. Science 275:805–807

897 Hirose N, Nishimura K, Yamamoto M (2009) Observational evidence of a warm ocean current
898 preceding a winter teleconnection pattern in the northwestern Pacific. Geophys Res Lett
899 36:L09705

900 Hirst AC (1986) Unstable and damped equatorial modes in simple coupled ocean-atmosphere
901 models. J Atmos Sci 43:606–630

902 Holland MM, Bailey DA, Briegleb BP, Light B, Hunke E (2012) Improved sea ice shortwave
903 radiation physics in CCSM4: The impact of melt ponds and aerosols on Arctic sea ice. J Clim
904 25:1413–1430

905 Hong CH, Cho KD, Kim HP (2001) The relationship between ENSO events and sea surface
906 temperature in the East (Japan) Sea. Prog Oceanogr 49:21–40

907 Hunke EC, Lipscomb WH (2008) CICE: The Los Alamos Sea Ice Model. Documentation and
908 Software User's Manual. Version 4.0. T-3 Fluid Dynamics Group, Los Alamos National
909 Laboratory, Tech Rep. LA-CC-06-012

910 Izumo T, and Coauthors (2010). Influence of the state of the Indian Ocean Dipole on the
911 following year's El Niño. Nature Geosci 3:168–172.

912 Izumo T, Lengaigne M, Vialard J, Luo JJ, Yamagata T, Madec G (2014) Influence of Indian
913 Ocean dipole and Pacific recharge on following year's El Niño: Interdecadal robustness. Clim
914 Dyn 42: 291–310

915 Jin FF (1997) An equatorial ocean recharge paradigm for ENSO. Part I: Conceptual model. J
916 Atmos Sci 54:811–829

917 Jo YH, Breaker LC, Tseng YH, Yeh SW (2014) A temporal multiscale analysis of the water off
918 the east coast of South Korea over the past four decades. Terr Atmos Ocean Sci *(in press)*

919 Kalnay E, and Coauthors (1996) The NCEP/NCAR 40-Year Reanalysis Project. Bull Amer
920 Meteor Soc 77:437–471

921 Kistler R, and Coauthors (2001) The NCEP–NCAR 50–Year Reanalysis: Monthly Means CD–
922 ROM and Documentation. Bull Amer Meteor Soc 82:247–267

923 Kug JS, Kang IS (2006) Interactive Feedback between ENSO and the Indian Ocean. J Clim
924 19:1784–1801

925 Kwon YO, and Coauthors (2010) Role of the Gulf Stream and Kuroshio–Oyashio systems in
926 large-scale atmosphere–ocean interaction: A review. J Clim 23:3249–3281

927 Lawrence DM, and Coauthors (2011) Parameterization improvements and functional and
928 structural advances in version 4 of the Community Land Model. J Adv Model Earth Syst
929 3:M03001 doi:10.1029/2011MS000045

930 Li C, Wu L (2013) Dynamic linkage between the north pacific and the tropical pacific:
931 Atmosphere-ocean coupling. Adv Atmos Sci 30:306–314

932 Li T, Wang B, Chang CP, Zhang Y (2003) A theory for the Indian Ocean dipole-zonal mode. J
933 Atmos Sci 60:2119–2135

934 Li Y, Lu R, Dong B 2007 The ENSO–Asian monsoon interaction in a coupled ocean–
935 atmosphere GCM. J Clim 20:5164–5177

936 Linkin ME, Nigam S (2008) The North Pacific Oscillation–West Pacific teleconnection pattern:
937 mature-phase structure and winter impacts. J Clim 21:1979–1997

938 Lindzen RS, Nigam S (1987) On the role of sea surface temperature gradients in forcing low
939 level winds and convergence in the tropics. J Atmos Sci 44:2418–2436

940 Liu Z, Wu L (2004) Atmospheric response to North Pacific SST: The role of ocean–atmosphere
941 coupling. J Clim 17:1859–1882

942 Luo JJ, Behera S, Masumoto Y, Sakuma H, Yamagata T (2008) Successful prediction of the
943 consecutive IOD in 2006 and 2007. Geophys Res Lett 35:L14S02

944 Mantua NJ, Hare SR, Zhang Y, Wallace JM, Francis R (1997) A Pacific interdecadal climate
945 oscillation with impacts on salmon production. Bull Amer Meteor Soc 78:1069–1079

946 Meinen CS, McPhaden MJ (2000) Observations of warm water volume changes in the equatorial
947 Pacific and their relationship to El Niño and La Niña. J Clim 13:3551–3559

948 Mehta VM, Fayos C (2005) Decadal variability of El Niño events in the northern hemisphere
949 winter and its impacts on the global climate. Workshop on Decadal Climate Variability,
950 Warrenton, VA, CRCES.

951 Neale R, Slingo J (2003) The maritime continent and its role in the global climate: A GCM
952 Study. J Clim 16:834–848

953 Neale RB, and Coauthors (2013) The mean climate of the Community Atmosphere Model (CAM4)
954 in forced SST and fully coupled experiments. J Clim 26: 5150-5168

955 Oleson KW and Coauthors (2010) Technical description of version 4.0 of the Community Land
956 Model (CLM). NCAR Technical Note NCAR/TN-478+STR, 257 pp

957 Pegion K, Alexander M (2013) The seasonal footprinting mechanism in CFSv2: simulation and
958 impact on ENSO prediction. Clim Dyn 41:1671–1683

959 Philander SGH, Yamagata T, Pacanowski RC (1984) Unstable air-sea interaction in the tropics. J
960 Atmos Sci 41:604–613

961 Picaut J, Masia F, Penhoat YD (1997) An advective-reflective conceptual model for the oscillatory
962 nature of the ENSO. Science 277:663–666

963 Qiu B (2002) Large-scale variability in the midlatitude subtropical and subpolar North Pacific
964 Ocean: Observations and causes. J Phys Oceanogr 32:353–375

965 Qiu B, Chen S (2010) Interannual variability of the north Pacific subtropical countercurrent and its
966 associated mesoscale eddy field. J Phys Oceanogr 40:213–225

967 Ramanathan V, Collins W (1991) Thermodynamic regulation of ocean warming by cirrus clouds
968 deduced from the 1987 El Niño. Nature 351:27–32

969 Rogers JC (1981) The North Pacific Oscillation. Int J Climatol 1:39–57

970 Schneider N, Miller AJ, Pierce DW (2002) Anatomy of North Pacific decadal variability. J Clim
971 15:586–605

972 Sardeshmukh PD, Hoskins BJ (1988) The generation of global rotational flow by steady
973 idealized tropical divergence. J Atmos Sci 45:1228–1251

974 Shen ML, Tseng YH, Jan S, Young CC, Chiou MD (2014) Long-term variability of the Kuroshio
975 transport east of Taiwan and the climate it conveys. Prog Oceanogr 121:60–73

976 Small RJ and Coauthors (2008) Air–sea interaction over ocean fronts and eddies. Dyn Atmos
977 Oceans 45:274–319

978 Smith TM, Reynolds RW, Peterson TC, Lawrimore J (2008) Improvements to NOAA's historical
979 merged land-ocean surface temperature analysis (1880-2006). J Clim 21:2283–2296

980 Solomon A, Jin FF (2005) A study of the impact of off-equatorial warm-pool SST anomalies on
981 ENSO cycles. J Clim 18:274–286

982 Suarez MJ, Schopf PS (1988) A delayed action oscillator for ENSO. J Atmos Sci 45:3283–3287

983 Takahashi K, Montecinos A, Goubanova K, Dewitte B (2011) ENSO regimes: Reinterpreting the
984 canonical and Modoki El Niño. Geophys Res Lett 38:L10704. doi:10.1029/2011GL047364

985 Torrence C, Compo GP (1998) A practical guide to wavelet analysis. Bull Amer Meteor Soc
986 79:61–78

987 Trenberth KE, Branstator GW, Karoly D, Kumar A, Lau NC, Ropelewski C (1998) Progress
988 during TOGA in understanding and modeling global teleconnections associated with tropical sea
989 surface temperatures. J Geophys Res 103:14291-14324

990 Tzeng WN, and Coauthors(2012) Evaluation of multi-scale climate effects on annual recruitment
991 levels of the Japanese Eel, *Anguilla japonica*, to Taiwan, PLoS ONE 7:e30805.
992 doi:10.1371/journal.pone.0030805

993 Vialard J, and Coauthors (2001) A model study of oceanic mechanisms affecting equatorial
994 Pacific sea surface temperature during the 1997–98 El Niño. J Phys Oceanogr 31:1649–1675

995 Vimont DJ, Wallace JM, Battisti DS (2003) The seasonal footprinting mechanism in the Pacific:
996 Implications for ENSO. J Clim 16:2668–2675

997 Vimont D J, Alexander M, Fontaine A (2009) Midlatitude excitation of tropical variability in the
998 Pacific: The role of thermodynamic coupling and seasonality. J Clim 22:518–534

999 Vimont D J (2010) Transient growth of thermodynamically coupled variations in the tropics
1000 under an equatorially symmetric mean state. J Clim 23:5771–5789

1001 Vivier F, Kelly KA, Thompson L (2002) Heat budget in the Kuroshio Extension region: 1993–99.
1002 J Phys Oceanogr 32:3436–3454

1003 Waliser DE, Graham NE (1993) Convective cloud systems and warm-pool SSTs: Coupled
1004 interactions and self-regulation. J Geophy Res 98:12881–12893

1005 Walker GT, Bliss EW (1932) World Weather V, Memoir. Roy Meteorol Soc 4:53–84

1006 Wang SY, L'Heureux M, Chia HH (2012) ENSO prediction one year in advance using western
1007 North Pacific sea surface temperatures. Geophys Res Lett 39:L05702.
1008 doi:10.1029/2012GL050909

1009 Wang H, Mehta VM (2008) Decadal variability of the Indo-Pacific warm pool and its association
1010 with atmospheric and oceanic variability in the NCEP-NCAR and SODA reanalyses. J Clim
1011 21:5545–5565

1012 Wang C, Picaut J (2013) Understanding Enso Physics—A Review. In: Wang C, Xie SP, Carton
1013 JA (ed) Earth's Climate, American Geophysical Union, Washington, D. C.. doi:
1014 10.1029/147GM02

1015 Wang C, Wang X (2013) Classifying El Niño Modoki I and II by different impacts on rainfall in
1016 Southern China and typhoon tracks. J Clim 26:1233–1388

1017 Wang B, Xie X (1998) Coupled modes of the warm pool climate system. Part I: The role of air–
1018 sea interaction in maintaining Madden–Julian Oscillation. J Clim 11:2116–2135

1019 Wyrtki K (1975) El Niño–The dynamic response of the equatorial Pacific Ocean to atmospheric
1020 forcing. J Phys Oceanogr 4:91–103

1021 Xie SP, Philander SGH (1994) A coupled ocean-atmosphere model of relevance to the ITCZ in
1022 the eastern Pacific. Tellus 46A:340–350

1023 Yu JY, Kim ST (2011) Relationships between extratropical sea level pressure variations and the
1024 central-Pacific and eastern-Pacific types of ENSO. J Clim 24:708–720

1025 Yuan D, and Coauthors (2011) Forcing of the Indian Ocean Dipole on the interannual variations of
1026 the tropical Pacific ocean: Roles of the Indonesian Throughflow. J Clim 24:3593–3608

1027 Yuan D, Zhou H, Zhao X (2013) Interannual climate variability over the tropical Pacific ocean
1028 induced by the Indian Ocean Dipole through the Indonesian Throughflow. J Clim 26:2845–2861

1029 Zebiak SE (1982) A simple model of relevance to El Niño. J Atmos Sci 39:2017–2027

1030 Zhang Y, Wallace JM, Battisti DS (1997) ENSO-like interdecadal variability: 1900-93. J Clim
1031 10:1004-1020

1032 Zhang W, Li J, Jin FF (2009) Spatial and temporal features of ENSO meridional scales. Geophys
1033 Res Lett 36:L15605. doi:10.1029/2009GL038672

Figure 1. The correlation of Niño4 index in the January(1) and Pacific SST anomalies at different lags from 1957-2010. The Niño4 index has lags of (a) 15 months; (b) 12 months; (c) 9 months; (d) 6 months; (e) 3 months; and (f) 0 months (no lag). Only $P<0.05$ is shown. The contours lines are correlations=0.6 (bold black), 0.5 (thin black) and 0.4 (grey).

Figure 2. The standard deviation of surface temperature (left panel) and surface wind stress (right panel) for the three numerical experiments. (a) and (d) are for the CESM control simulation (top); (b) and (e) are for the $Wind_{clim}$ simulation; and (c) and (f) are for the SST_{clim} simulation. The black box shows the region where the wind or SST climatology is forced. The standard deviation of surface temperature (TS) and surface wind stress (TAU) in the black box are labeled.

Figure 3. Scatter diagram of averaged zonal wind speed (or stress) v.s. Niño4 SST anomalies (160°E–150°W), normalized by their respective standard deviations from the observation and CESM simulations.

Figure 4. The monthly averaged difference between the two experiments and the control simulation in the defined IPWP region: (a) SST, (b) surface temperature, (c) latent heat flux, (d) sensible heat flux, (e) evaporation flux, (f) precipitation rate, (g) 10m wind speed, (h) ocean surface zonal velocity and (i) ocean surface meridional velocity.

Figure 5. The covariability mode of SLP anomalies and SST anomalies (9-month running mean) from the CEOF analysis in the North Pacific. The columns from left to right are observation, CESM control, $Wind_{clim}$, SST_{clim}, respectively. The 1^{st} and 2^{nd} rows are the 1^{st} mode of SLPA and SSTA. The 3^{rd} and 4^{th} rows are the 2^{nd} mode.

Figure 6. Lag-correlation between Niño3 (and EMI index) and PC1/PC2 of the combined EOF (nine-month running mean). Positive (negative) axis means Niño3 (and EMI index) lags (leads).

Figure 7: Wavelet power spectrum (left) and global power spectrum (right) of PC1 (colors) and PC2 (black contour lines) from the observation and CESM experiments. The local wavelet power spectrum provides a measure of the variance distribution of the time series according to time and periodicity; high variability is represented by red, whereas blue indicates a weak variability in the wavelet power spectrum. For the global power spectrum, the dashed lines indicate 95% significant level and the periods of 3, 5 and 12 year, respectively.

Figure 8: the correlation maps between the December-February (DJF) PC2 and SST anomalies for DJF and several lead times (MAM, JJA, SON and DJF+1) based on the observation and CESM simulations.

Figure 9: The averaged negative meridional gradient of SST (*-dSST/dy*) during November-May in the (a) observation and (b) CESM control simulation. CEOF2 SST anomalies in Fig. 5 are also superimposed as contours. The SST anomalies covered by the rectangular box are used for further composite analysis.

Figure 10: The areal averaged meridional SST gradient (*-dSST/dy*) in the (a) observation and (b) CESM control simulation. The dashed lines show 1 standard deviation (std). The analysis region is the rectangular box of Fig. 9.

Figure 11: The composites of SLP anomalies during November-May (NDJFMAM) at different lag times (ranging from SLP leading by 3 months to SLP lagged by 4 months) for the positive phase of the meridional SST gradient shown in Fig. 10 (amplitude is greater than 1 std). The patterns of NPO are superimposed as contours (positive anomalies are solid lines and the negative anomalies are dashed lines).

Figure 12: same as Fig. 11 but the amplitude is less than -1 std (negative phase).

Figure 13: The composites of LHF during November-May (NDJFMAM) at different lag times (ranging from SLP leading by 3 months to SLP lagged by 4 months) for the negative phase of the meridional SST gradient shown in Fig. 10 (amplitude is less than -1).

Figure 14: the composites of vertical velocity Ω (*Pa/s*, negative upward and positive downward) and streamlines for the same negative phase (amplitude is less than -1) of the meridional SST gradient along the vertical section averaged between 30°N and 45°N. The vertical velocity in the streamline is normalized by -1000 in order to be comparable with horizontal velocity scale with positive upward.

Figure 15: same as Fig. 14 but for the vertical section averaged between 120°E and 150°E. The vertical velocity in the streamline is normalized by -200 in order to be comparable with horizontal velocity scale with positive upward.

Figure 16: The dynamical processes in associated with Kuroshio pathway.

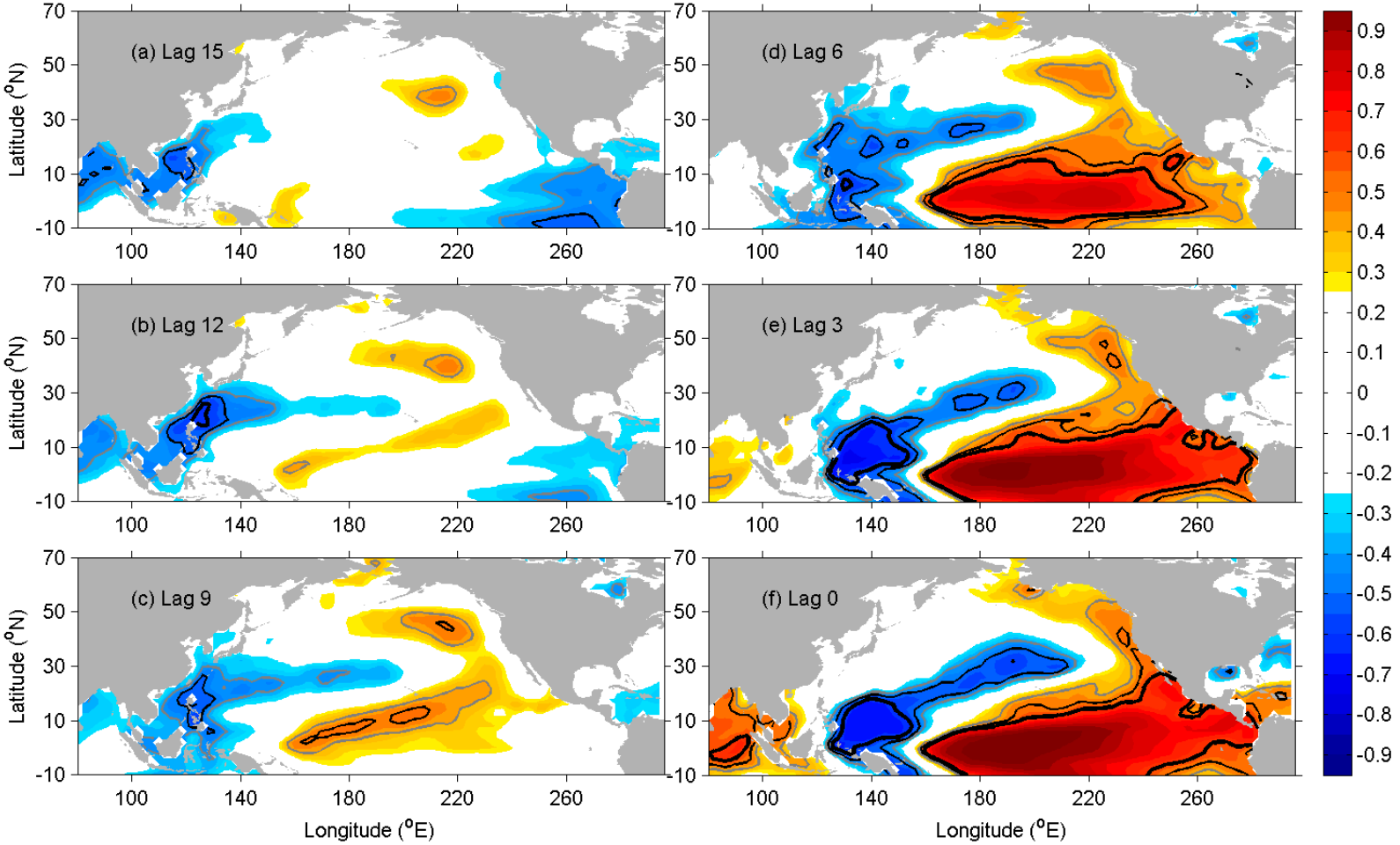

Figure 1. The correlation of Niño4 index in the January(1) and Pacific SST anomalies at different lags from 1957-2010. The Niño4 index has lags of (a) 15 months; (b) 12 months; (c) 9 months; (d) 6 months; (e) 3 months; and (f) 0 months (no lag). Only $P<0.05$ is shown. The contours lines are correlations=0.6 (bold black), 0.5 (thin black) and 0.4 (grey).

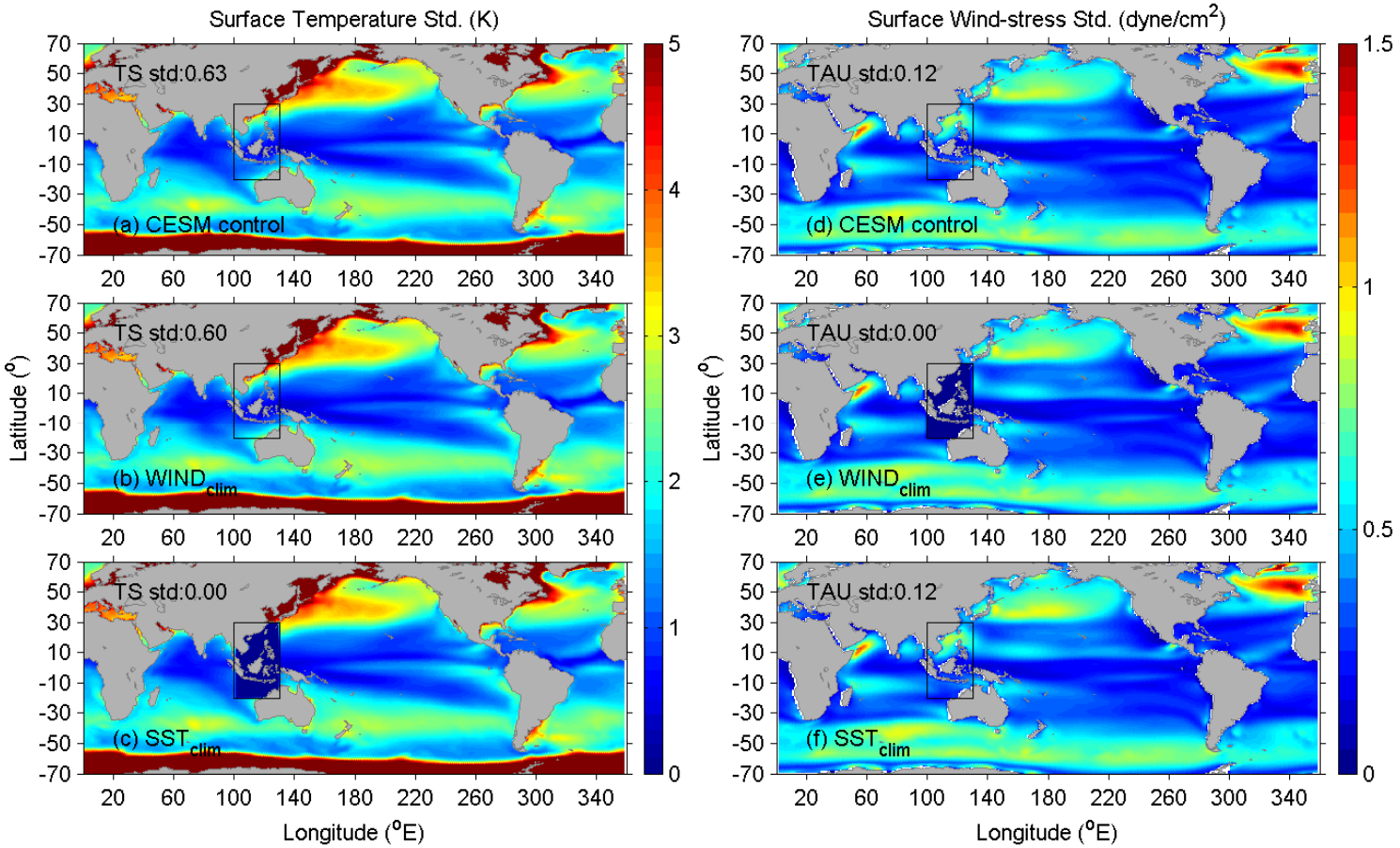

Figure 2. The standard deviation of surface temperature (left panel) and surface wind stress (right panel) for the three numerical experiments. (a) and (d) are for the CESM control simulation (top); (b) and (e) are for the $Wind_{clim}$ simulation; and (c) and (f) are for the SST_{clim} simulation. The black box shows the region where the wind or SST climatology is forced. The standard deviation of surface temperature (TS) and surface wind stress (TAU) in the black box are labeled.

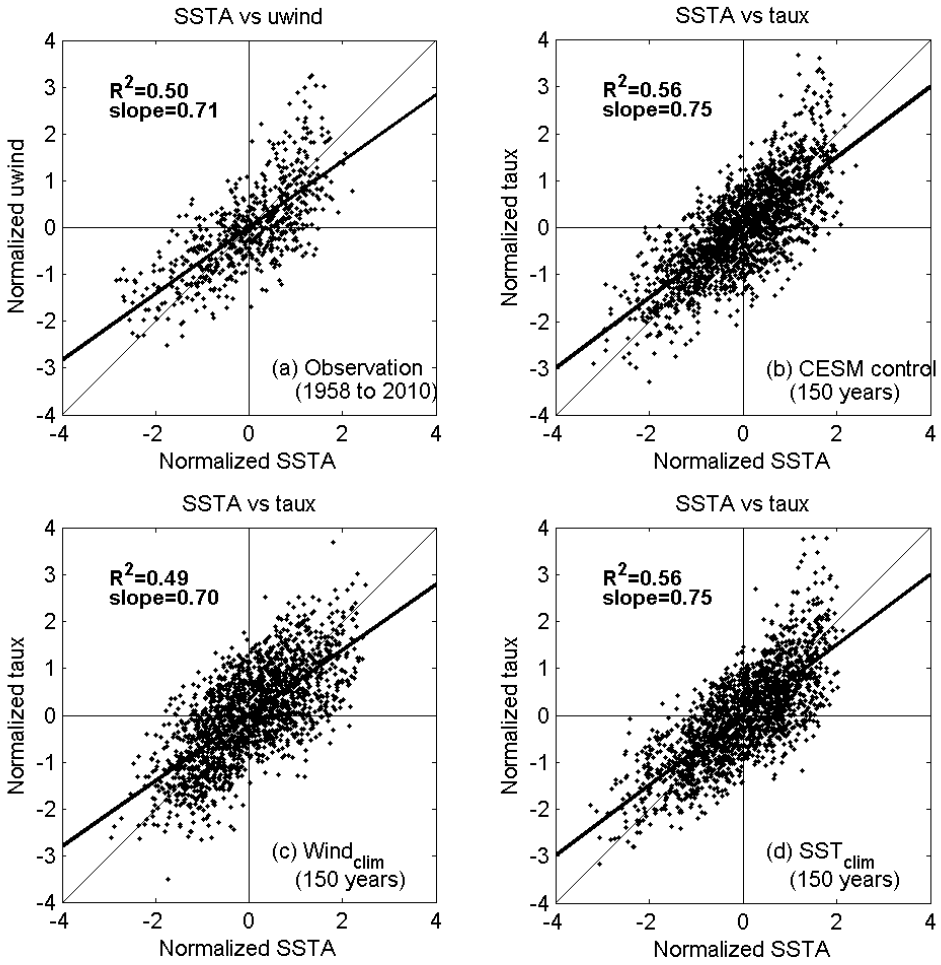

Figure 3. Scatter diagram of averaged zonal wind speed (or stress) v.s. Niño4 SST anomaly (190°–240°E), normalized by their respective standard deviations from the observation and CESM simulations.

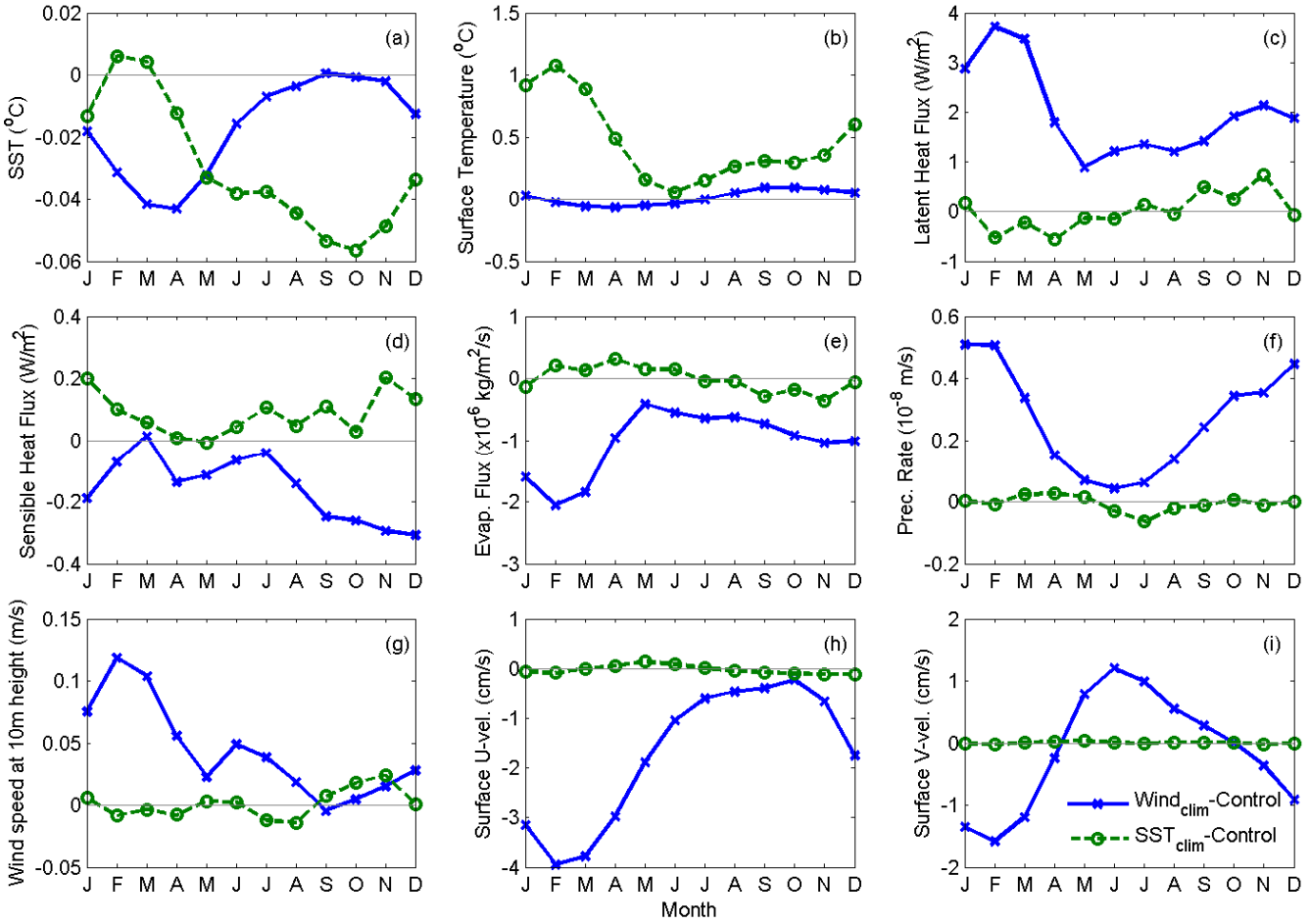
(a)
SST (°C)
(b)
Surface Temperature (°C)
(c)
Latent Heat Flux (W/m²)
(d)
Sensible Heat Flux (W/m²)
(e)
Evap. Flux (x10⁻⁶ kg/m²/s)
(f)
Prec. Rate (10⁻⁸ m/s)
(g)
Wind speed at 10m height (m/s)
(h)
Surface U-vel. (cm/s)
(i)
Surface V-vel. (cm/s)
J F M A M J J A S O N D
Month
Wind_clim-Control
SST_clim-Control

Figure 4. The monthly averaged difference between the two experiments and the control simulation in the defined IPWP region: (a) SST, (b) surface temperature, (c) latent heat flux, (d) sensible heat flux, (e) evaporation flux, (f) precipitation rate, (g) 10m wind speed, (h) ocean surface zonal velocity and (i) ocean surface meridional velocity.

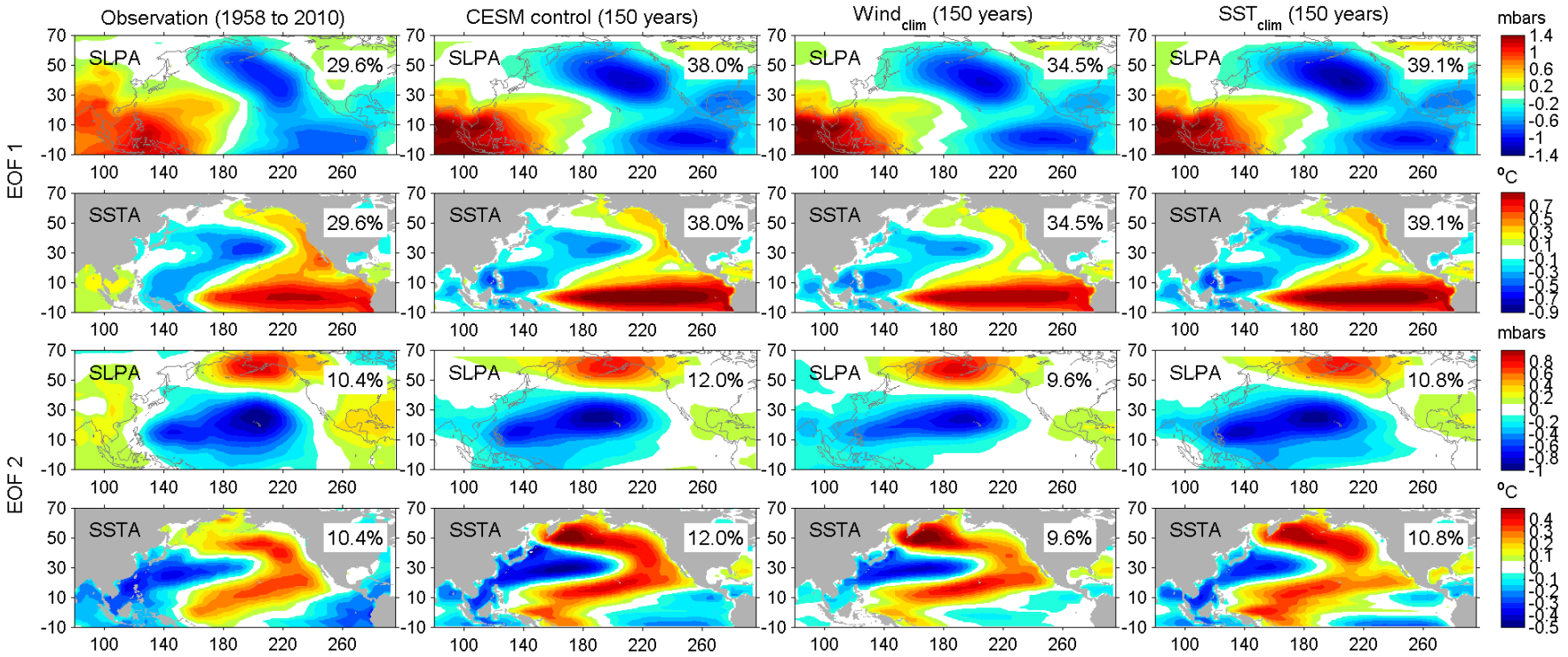

Figure 5. The covariability mode of SLP anomalies and SST anomalies (9-month running mean) from the CEOF analysis in the North Pacific. The columns from left to right are observation, CESM control, $Wind_{clim}$, SST_{clim}, respectively. The 1st and 2nd rows are the 1st mode of SLPA and SSTA. The 3rd and 4th rows are the 2nd mode.

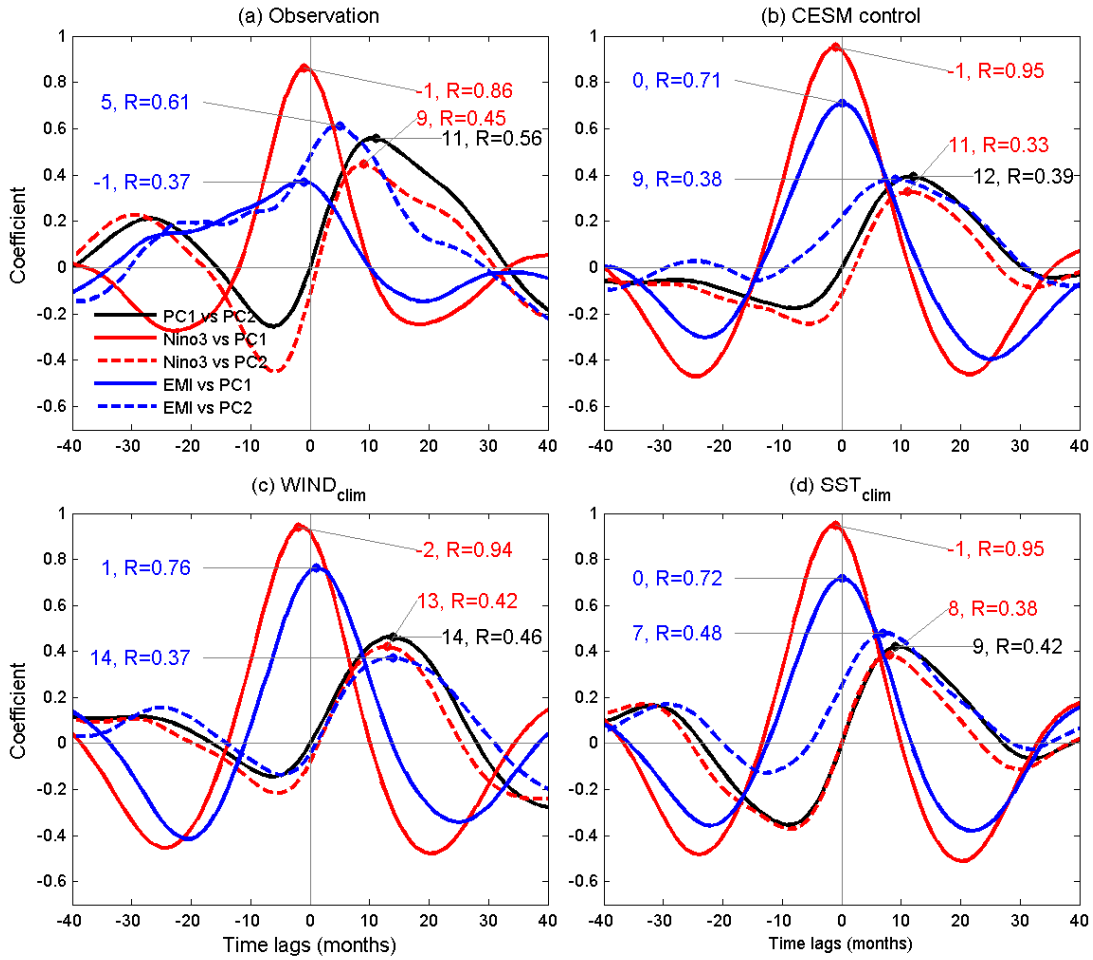

Figure 6. Lag-correlation between Niño3 (and EMI index) and PC1/PC2 of the combined EOF (nine-month running mean). Positive (negative) axis means Niño3 (and EMI index) lags (leads).

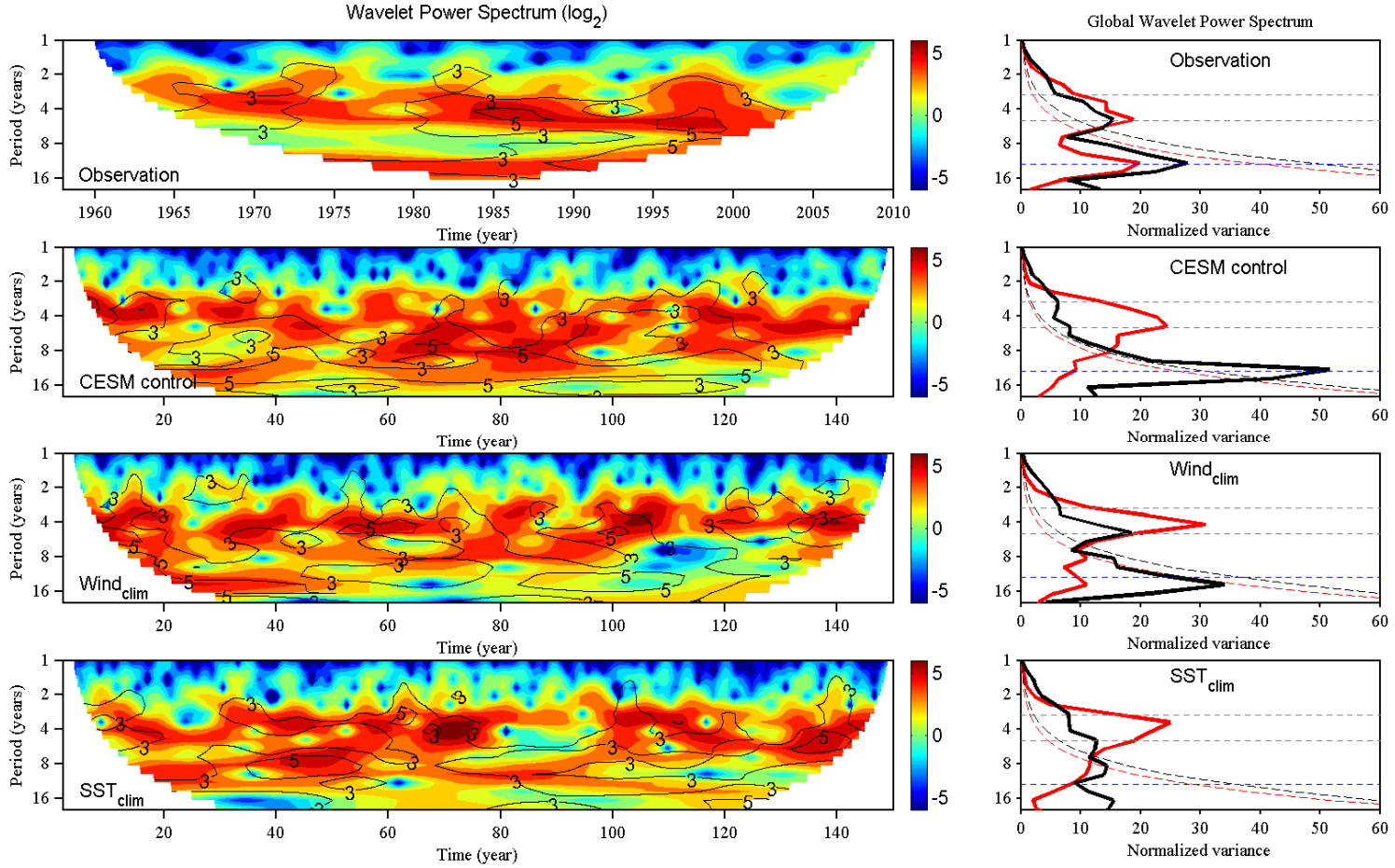

Figure 7: Wavelet power spectrum (left) and global power spectrum (right) of PC1 (colors) and PC2 (black contour lines) from the observation and CESM experiments. The local wavelet power spectrum provides a measure of the variance distribution of the time series according to time and

periodicity; high variability is represented by red, whereas blue indicates a weak variability in the wavelet power spectrum. For the global power spectrum, the dashed lines indicate 95% significant level and the periods of 3, 5 and 12 year, respectively.

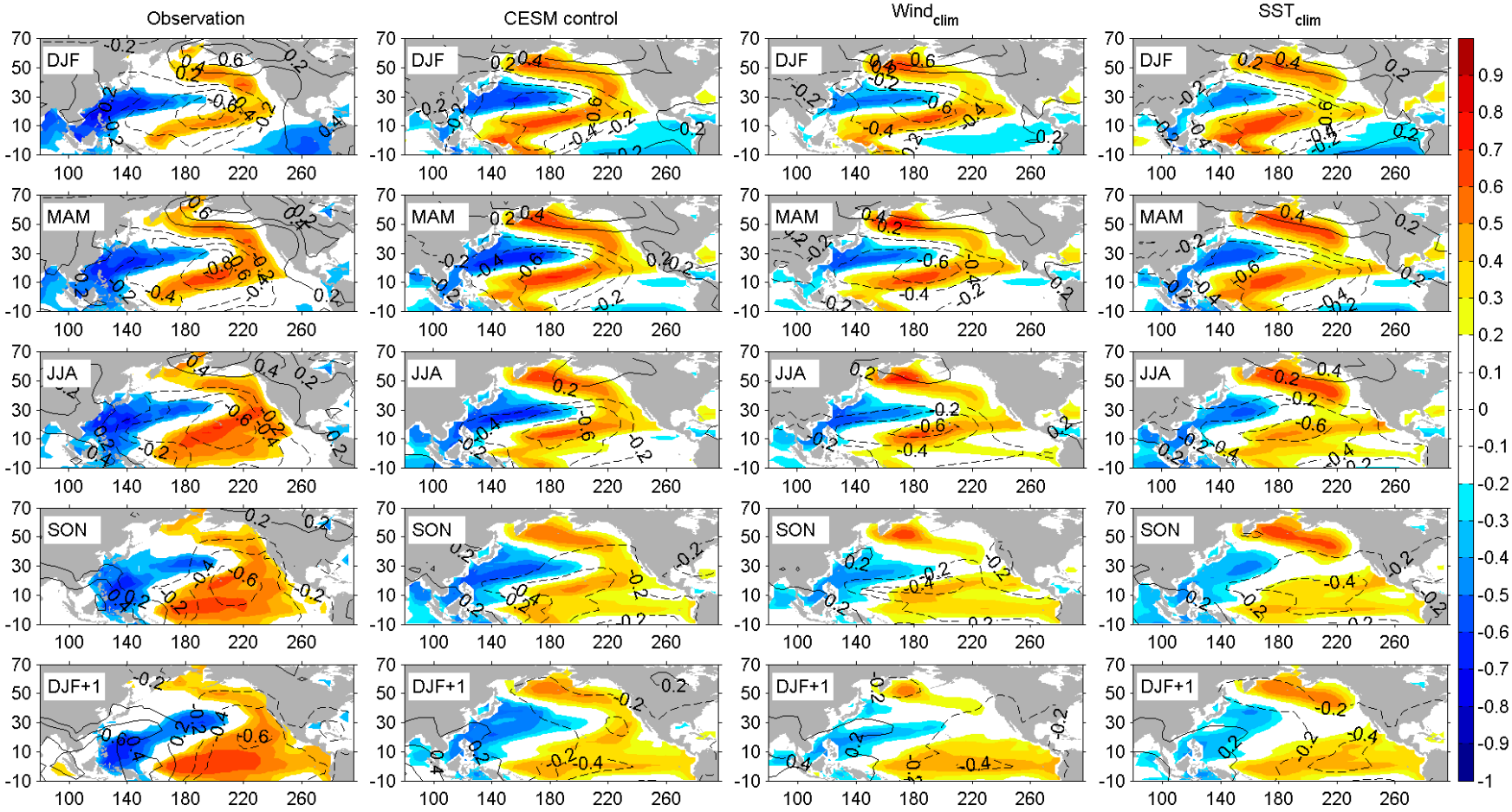

Figure 8: the correlation maps between the December-February (DJF) PC2 and SST anomalies for DJF and several lead times (MAM, JJA, SON and DJF+1) based on the observation and CESM simulations.

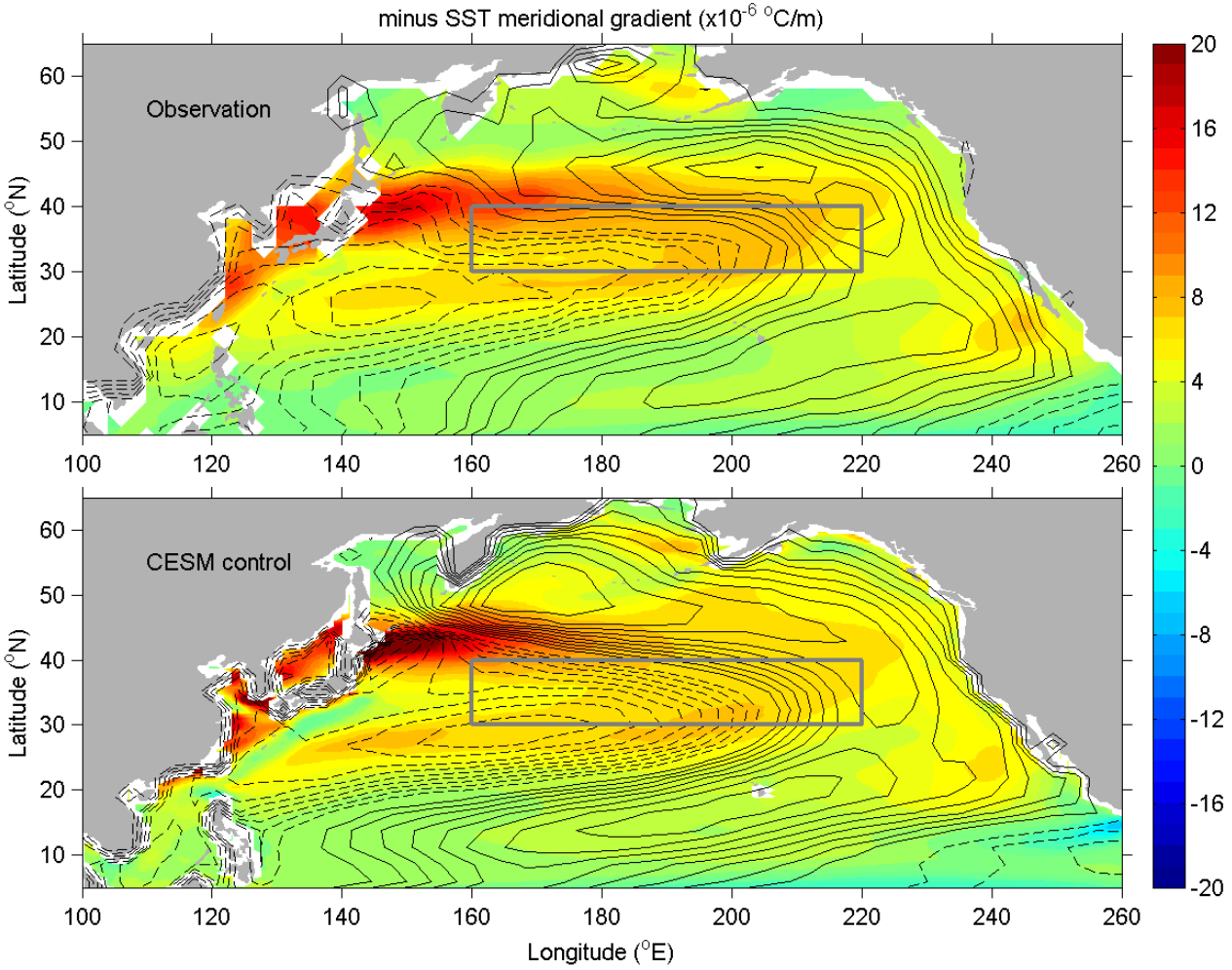

Figure 9: The averaged negative meridional gradient of SST (*-dSST/dy*) during November-May in the (a) observation and (b) CESM control simulation. CEOF2 SST anomalies in Fig. 5 are also superimposed as contours. The SST anomalies covered by the rectangular box are used for further composite analysis.

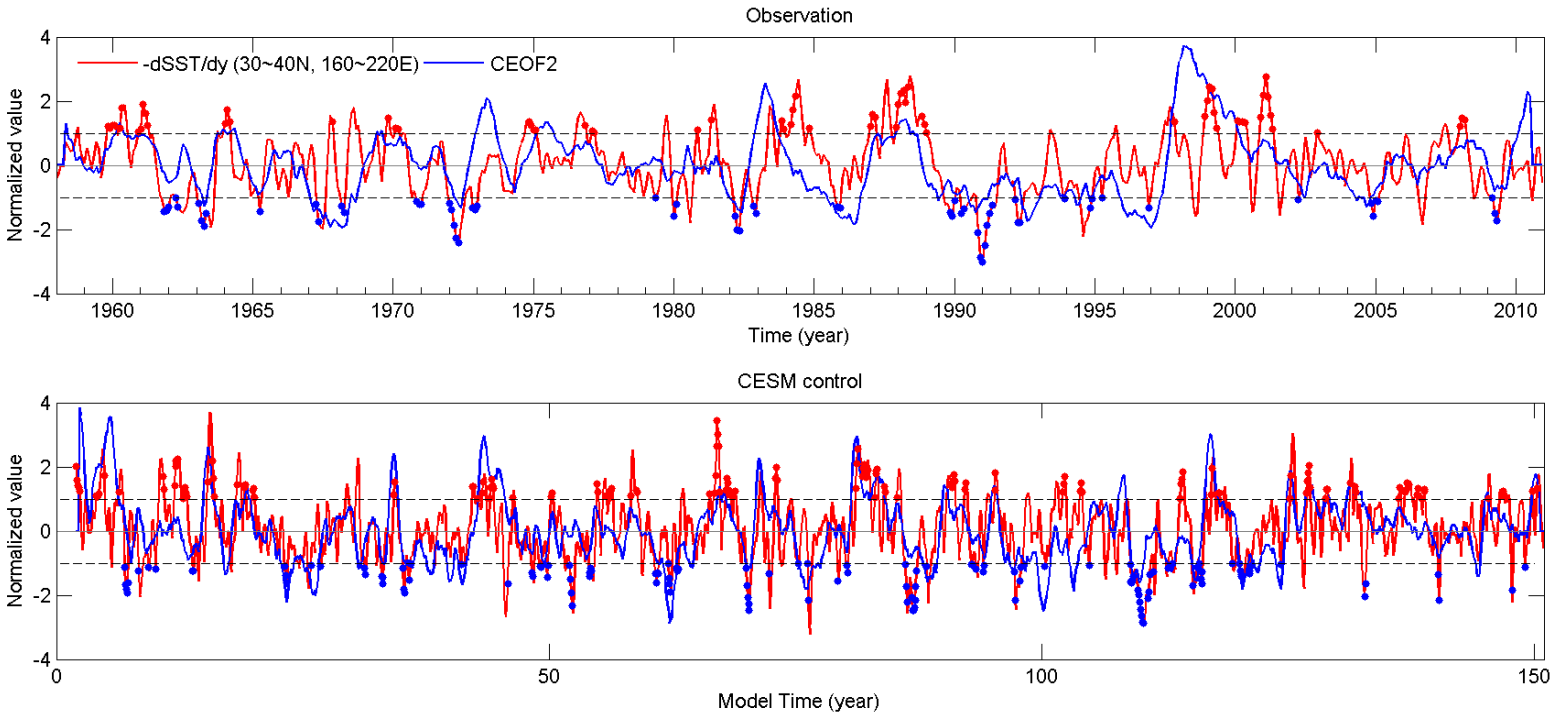

Figure 10: The areal averaged meridional SST gradient (*-dSST/dy*) in the (a) observation and (b) CESM control simulation. The dashed lines show 1 standard deviation (std). The analysis region is the rectangular box of Fig. 9.

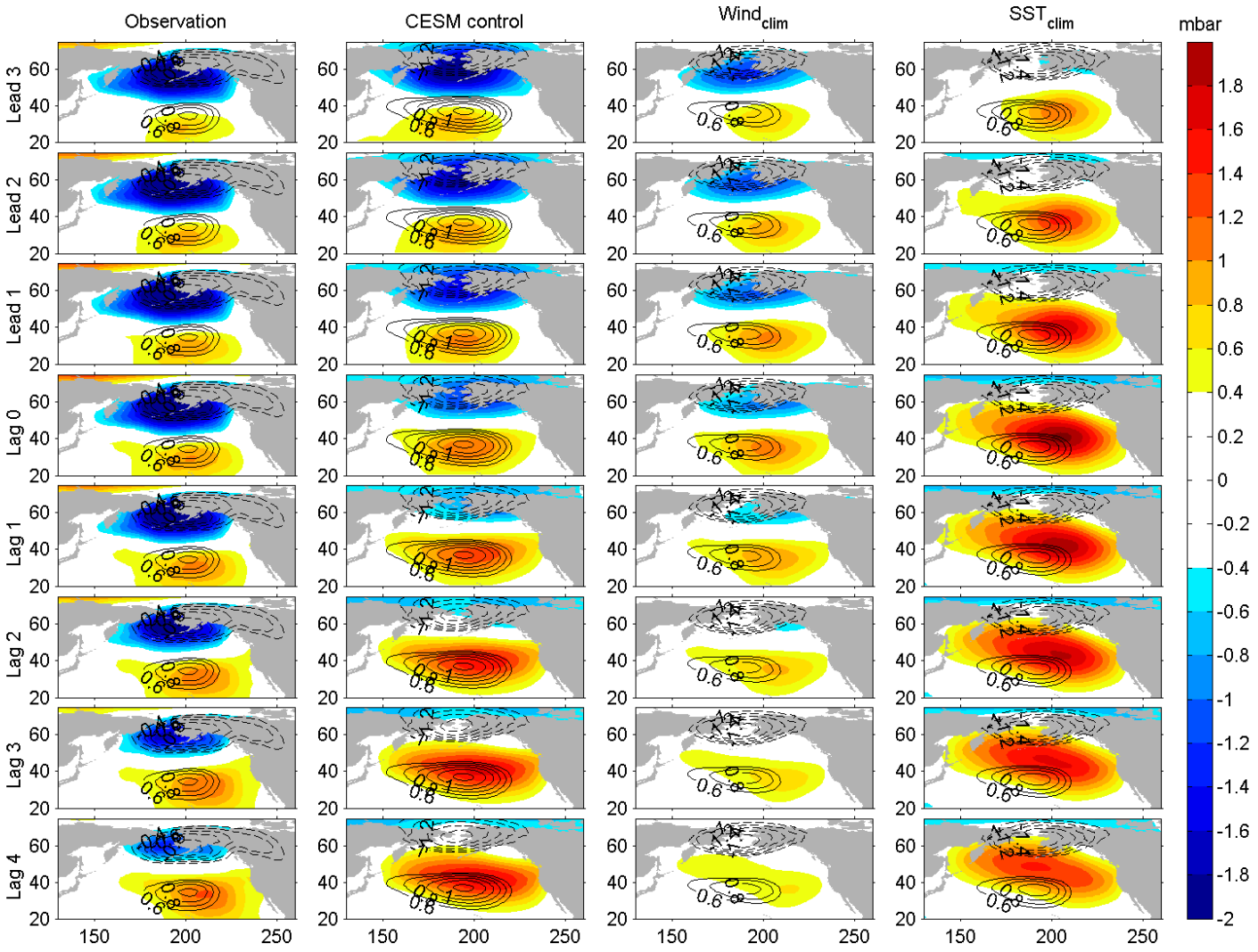
Observation
CESM control
Wind clim
SST clim
mbar
Lead 3
Lead 2
Lead 1
Lag 0
Lag 1
Lag 2
Lag 3
Lag 4
20
40
60
150
200
250
1.8
1.6
1.4
1.2
1
0.8
0.6
0.4
0.2
0
-0.2
-0.4
-0.6
-0.8
-1
-1.2
-1.4
-1.6
-1.8
-2

Figure 11: The composites of SLP anomalies during November-May (NDJFMAM) at different lag times (ranging from SLP leading by 3 months to SLP lagging by 4 months) for the positive phase of the meridional SST gradient shown in Fig. 10 (amplitude is greater than 1 std). The patterns of NPO are superimposed as contours (positive anomalies are solid lines and the negative anomalies are dashed lines).

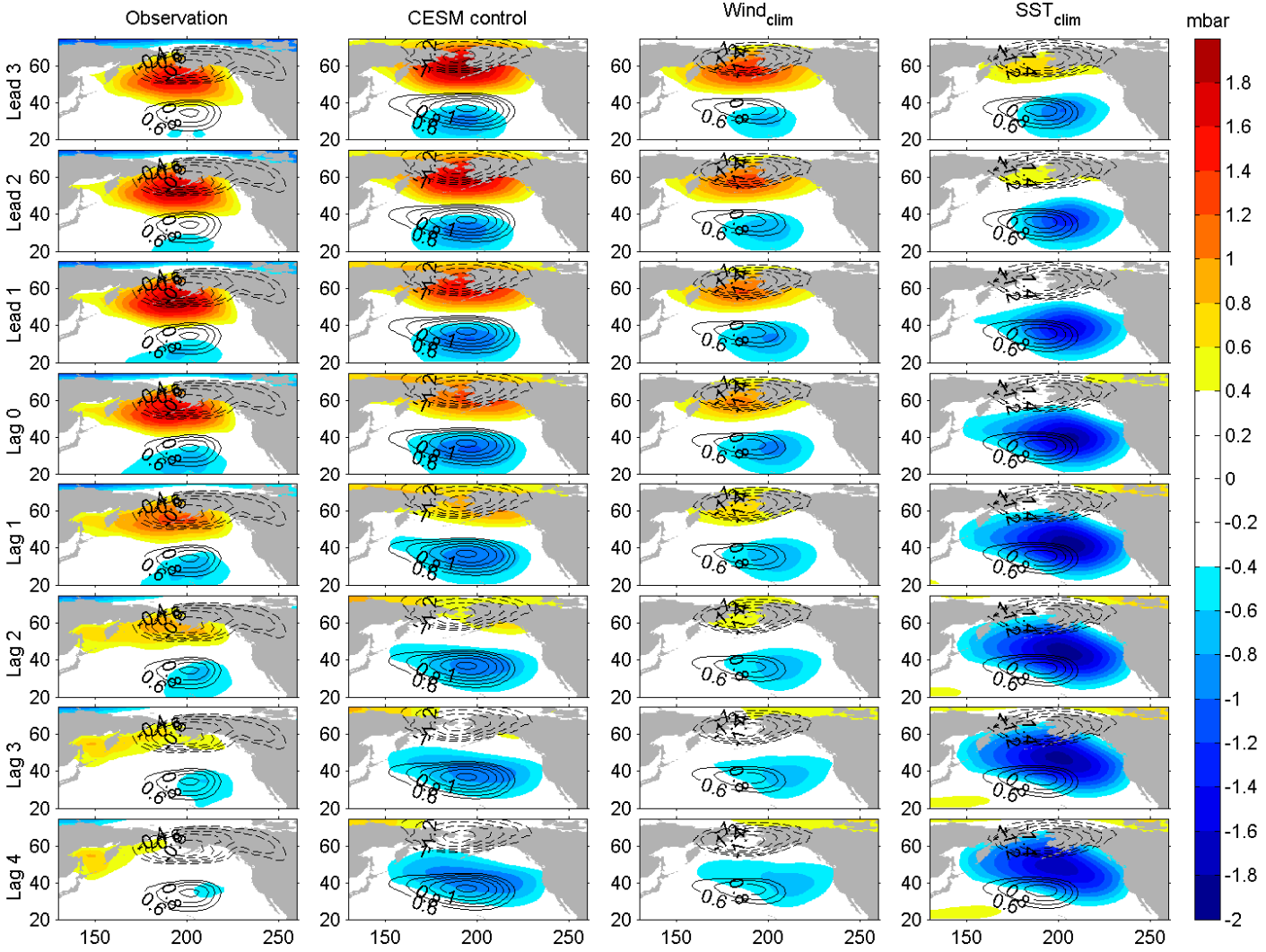

Figure 12: same as Fig. 11 but the amplitude is less than -1 std (negative phase).

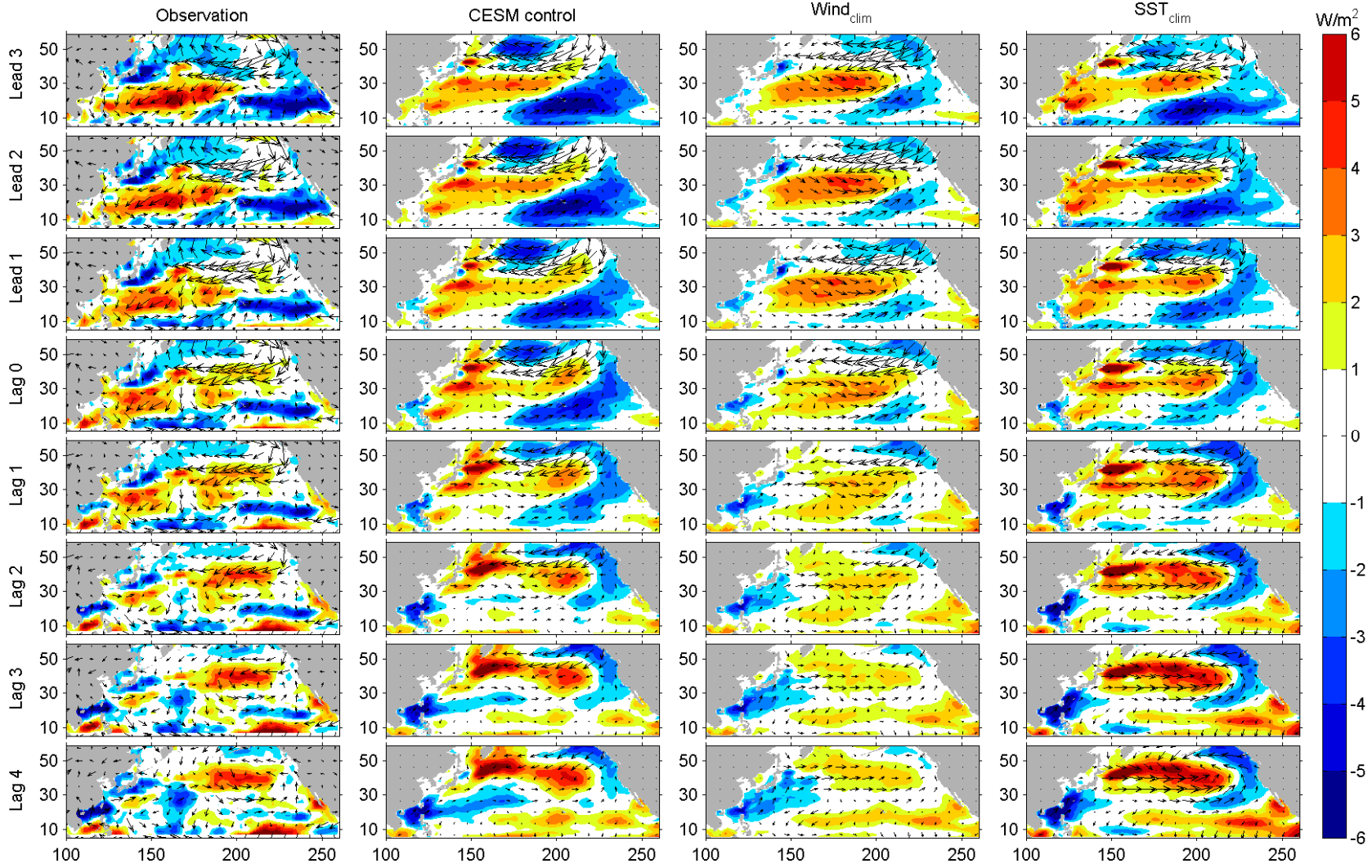

Figure 13: The composites of LHF during November-May (NDJFMAM) at different lag times (ranging from SLP leading by 3 months to SLP lagging by 4 months) for the negative phase of the meridional SST gradient shown in Fig. 10 (amplitude is less than -1).

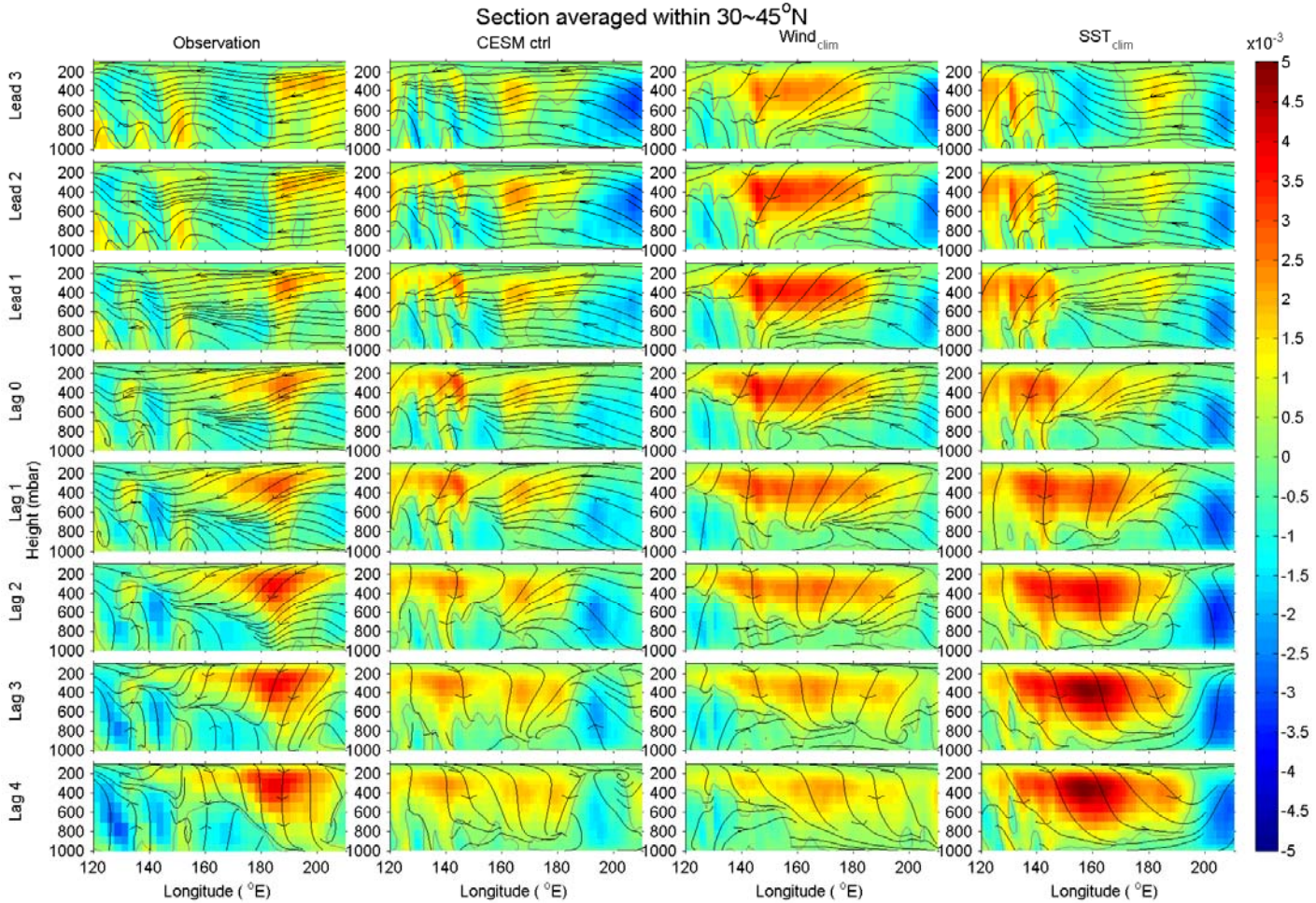

Figure 14: the composites of vertical velocity Ω (negative upward and positive downward) and streamlines for the same negative phase (amplitude is less than -1) of the meridional SST gradient along the vertical section averaged between 30°N and 45°N. The vertical velocity in the streamline is normalized by -1000 in order to be comparable with horizontal velocity scale with positive upward.

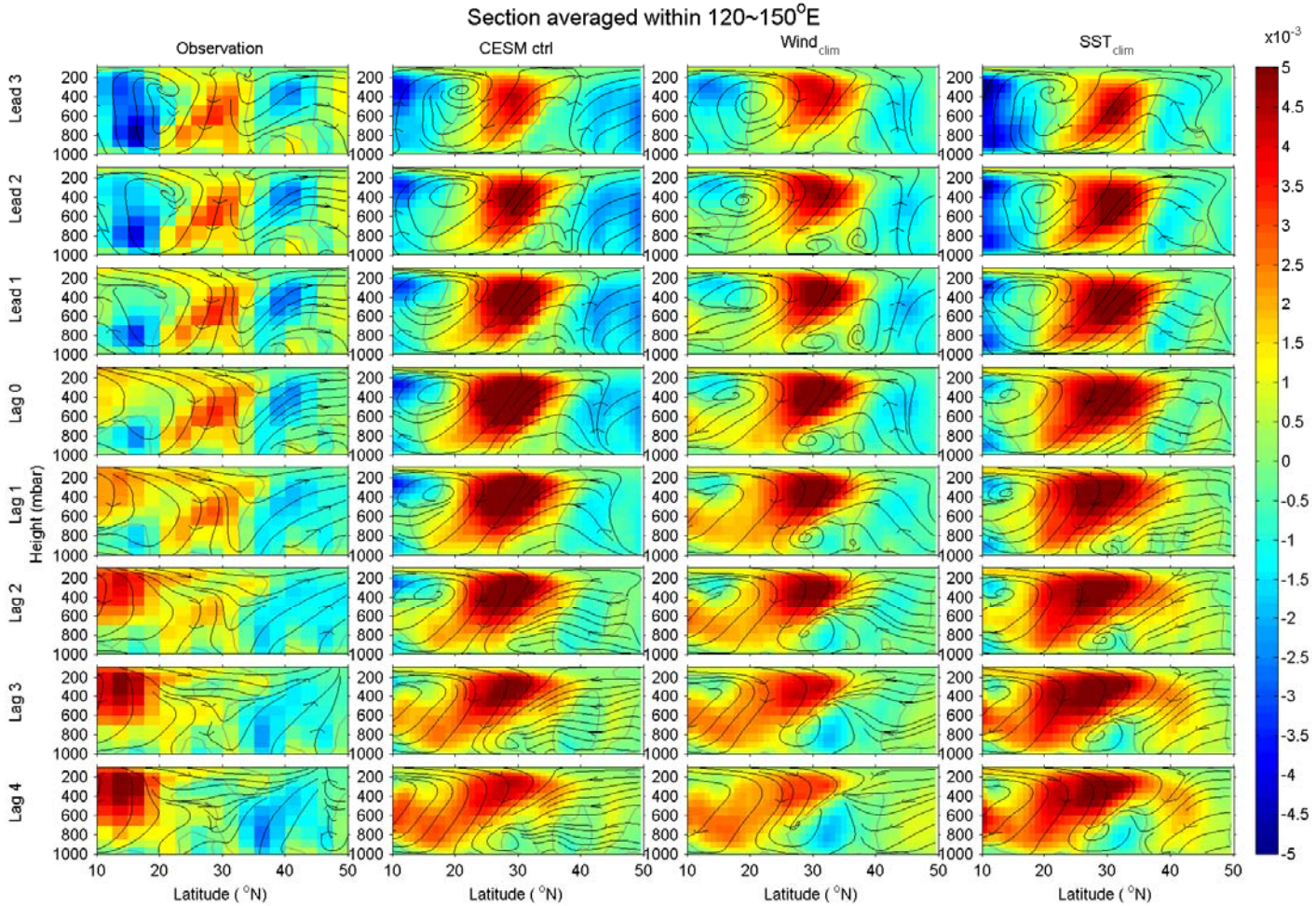

Figure 15: same as Fig. 14 but for the vertical section averaged between 120°E and 150°E. The vertical velocity in the streamline is normalized by -200 in order to be comparable with horizontal velocity scale with positive upward.

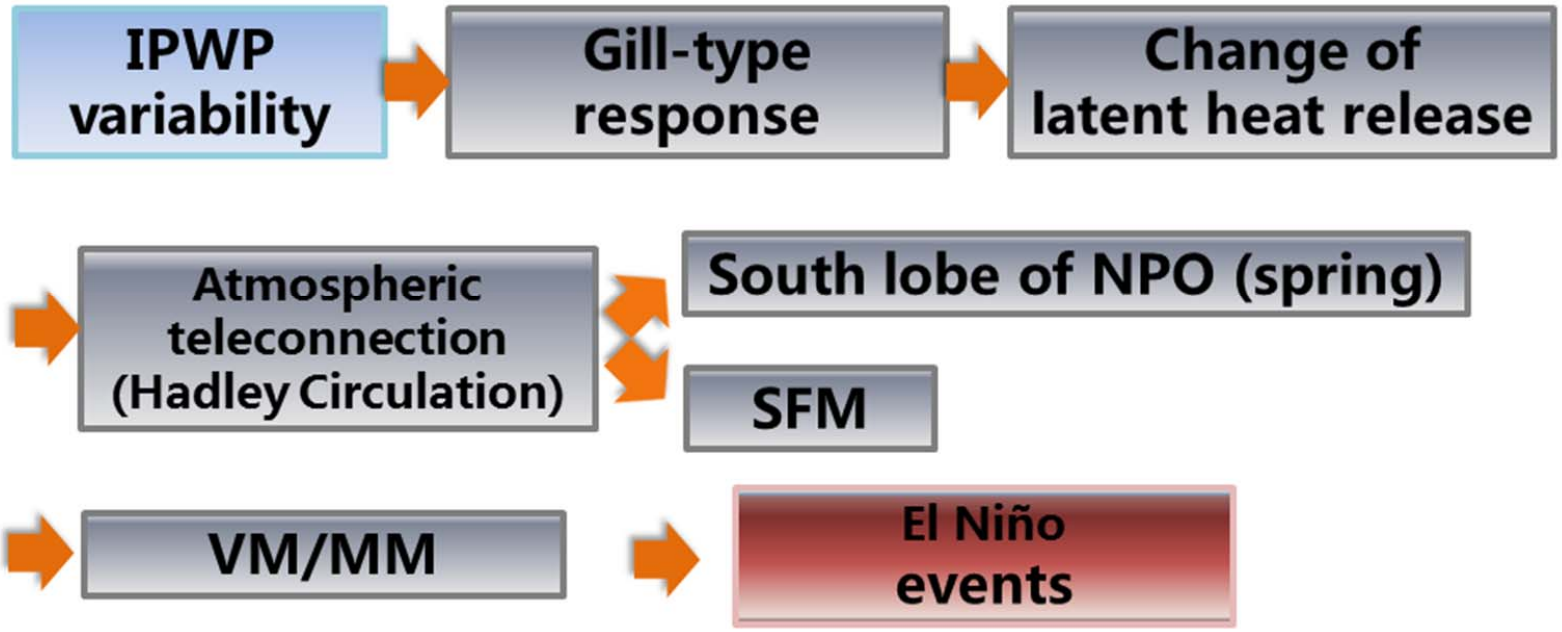

Figure 16: The dynamical processes in associated with Kuroshio pathway.